Analyzing the 21-cm signal brightness temperature in the Universe with inhomogeneities

Shashank Shekhar Pandey,* Ashadul Halder,† and A. S. Majumdar‡

Department of Astrophysics and High Energy Physics, S. N. Bose National Centre for Basic Sciences, Block JD, Sector III, Salt Lake, Kolkata-700106, India

(Received 10 November 2023; accepted 30 July 2024; published 28 August 2024)

We explore the 21-cm signal in our Universe containing inhomogeneous matter distribution at considerably large scales. Employing Buchert's averaging procedure in the context of a model of spacetime with multiple inhomogeneous domains, we evaluate the effect of our model parameters on the observable 21-cm signal brightness temperature. Our model parameters are constrained through the Markov chain Monte Carlo method using the Union 2.1 supernova Ia observational data. We find that a significant dip in the brightness temperature compared to the Λ cold dark matter prediction could arise as an effect of the inhomogeneities present in the Universe.

DOI: 10.1103/PhysRevD.110.043531

I. INTRODUCTION

For quite some time now, 21 cm cosmology has been an essential tool in studying the physics of the cosmic dark age [1–3]. It is a unique probe of the reionization epoch of the Universe [4,5]: 21 cm is the wavelength corresponding to the energy shift due to hyperfine splitting in the ground state of neutral hydrogen, the most abundant element in the Universe. It occupies ∼75% of the entire baryonic allocation of the Universe. The transition between hydrogen atoms' electronic spin states (s = 0,1) generates the 21-cm (∼1.42 GHz) hyperfine spectrum.

The brightness temperature T_{21} associated with this spectrum is a function of $T_s - T_\gamma$ where T_γ is the cosmic microwave background temperature given by $T_\gamma = 2.725(1+z)K$ and T_s is the spin temperature [1–3]. Recently, the "Experiment to Detect the Global Epoch of Re-ionization Signature" (EDGES) [6] generated quite a bit of excitement in the field with its reported T_{21} in the redshift range $14 < z < 20$ to be -500^{+200}_{-500} mK. However, the subsequent SARAS experiment [7] failed to detect the EDGES 21-cm signal [8].

The Λ cold dark matter (ΛCDM) model of standard cosmology estimates a brightness temperature of about ≈ -200 mK without any additional thermal contribution. To account for any additional cooling, various phenomenological effects in the early Universe have been employed [9–14], including exotic models of dark matter [11,13,15] and dark energy [16]. The 21-cm signal provides an avenue towards discerning several physical phenomena of this epoch, such as evaporating primordial black holes [9,12,14,17], baryon-dark matter scattering [11,13,15], and neutrino physics [18].

Although the ΛCDM model has been highly successful in establishing the basic tenets of standard cosmology, it has been confronted with certain discordant observations in recent times, notably among them the so-called Hubble tension [19,20]. Moreover, recent observations of large-scale structures indicate the scope of including additional features within the framework of standard cosmology. Although the Universe may be uniform and isotropic at the largest scales, various astrophysical surveys have revealed prominent matter distribution inhomogeneities up to slightly smaller scales [21]. Significant (more than 3σ) deviations from the ΛCDM mock catalogs have been reported [22] on luminous red galaxy samples as large as 500 h^{-1} Mpc. Recently, a giant arc of galaxies spanning ∼1 Gpc (proper size, present epoch) has been observed [23].

Such observed deviations in large-scale structures from the assumed smooth homogeneous ΛCDM paradigm may necessitate the inclusion of the impact of inhomogeneities in the analyses of cosmological phenomena. An averaging procedure is required to incorporate the effect of inhomogeneities in the analysis. Various averaging schemes have been proposed in the literature [24–28]. Buchert introduced a simplified averaging procedure [29,30] restricted to scalar quantities on spacelike hypersurfaces. Several studies employing the Buchert averaging procedure have been done to investigate the effect of backreaction of inhomogeneities on cosmological dynamics, including attempts to explain the current accelerated expansion of the Universe without invoking exotic physics [29–55].

Buchert's averaging procedure for evaluating the effect of backreaction of matter distribution inhomogeneities

*Contact author: shashankpandey7347@gmail.com
†Contact author: ashadul.halder@gmail.com
‡Contact author: archan@bose.res.in

offers the prospect of relating theoretically calculated spatially averaged quantities to observationally measurable quantities, such as redshift-distance relations [41,42,56–59]. Analyses of light wave propagation in the presence of inhomogeneities have revealed interesting features in the modified redshift-distance relation due to the backreaction effect [41,42,58]. Similar effects have also been derived in the context of gravitational waves emitted from compact binaries propagating through the inhomogeneous matter distribution [48,49]. In the present work, we are thus motivated to explore the 21-cm signal under the impact of backreaction from matter inhomogeneities employing the Buchert averaging framework.

Specifically, in the present analysis, we employ a model of spacetime with a spectrum of matter distribution inhomogeneities in multiple domains, which can imitate our actual Universe more realistically compared to earlier analyses of cosmological dynamics under backreaction, which have primarily relied on toy two-domain models [41,45–48]. We aim to theoretically analyze the 21-cm signal in the context of modified Hubble dynamics due to the effect of backreaction from matter distribution inhomogeneities evaluated using the Buchert formalism. We constrain our model parameters by performing Markov chain Monte Carlo analysis using the Union 2.1 supernova Ia data to determine the model parameters' best fit and optimum values. We compute the 21-cm brightness temperature, which reveals a significant dip compared to the ΛCDM prediction in the redshift range $14 < z < 20$, without invoking any additional nonstandard cosmological effects or exotic physics.

The paper is organized as follows. We briefly introduce the formalism for evaluating the 21-cm signal brightness temperature in Sec. II. Next, we briefly outline Buchert's averaging procedure in Sec. III. Our model of multidomain inhomogeneities is presented, leading to modified Hubble dynamics in Sec. IV. We then present our analysis of the 21-cm signal in the context of our multidomain model in Sec. V. In Sec. VI, we use the Union 2.1 supernova Ia data to constrain our model parameters and compute the 21-cm brightness temperature in the redshift range $14 < z < 20$ using the best fit and optimum values of our model parameters. Finally, we summarize our results in Sec. VII.

II. 21-CM BRIGHTNESS TEMPERATURE

The 21-cm absorption line of the hydrogen atom is generated by the transition of an electron between the two hyperfine spin states (spin 0 and spin 1). This 21-cm line has a characteristic temperature associated with it called the brightness temperature, T_{21}, which represents the intensity of the 21-cm line as a function of the cosmological redshift z. The expression for T_{21} is given by [10,60]

$$T_{21} = \frac{T_s - T_\gamma}{1+z}(1 - e^{-\tau(z)}), \tag{1}$$

where T_s is the 21-cm spin temperature at redshift z, T_γ is the cosmic microwave background temperature ($T_\gamma = 2.725(1+z)K$) and $\tau(z)$ is the optical depth of the intergalactic medium. $\tau(z)$ is given by [60]

$$\tau(z) = \frac{3}{32\pi}\frac{T_*}{T_s} n_{HI}\lambda_{21}^3 \frac{A_{10}}{H(z) + (1+z)\delta_r v_r}, \tag{2}$$

where $T_* = hc/(k_B\lambda_{21}) = 0.068$ K, $A_{10} = 2.85 \times 10^{-15}$ s^{-1} is the Einstein coefficient [61], $\lambda_{21} \approx 21$ cm, n_{HI} is the local neutral hydrogen density, $H(z)$ is the Hubble parameter and $\delta_r v_r$ is the radial gradient of the peculiar velocity. The above equations are derived from the principles of atomic physics and radiative transfer. The expression for optical depth has a term for the gradient of the proper velocity along the line of sight, and this term includes both the Hubble expansion and the peculiar velocity, as can be seen in Eq. (2) [1]. This is how $H(z)$, the Hubble parameter, which measures the Universe's rate of expansion, enters the analysis. Since $H(z)$ itself depends on the model of cosmology, the values of the quantities of interest turn out to be different for different models of cosmology.

The spin temperature T_s is related to the ratio of the number density of hydrogen atoms in excited and ground states and is given by [60]

$$\frac{n_1}{n_0} = 3e^{-T_*/T_s}, \tag{3}$$

where n_1 and n_0 are the number densities of hydrogen atoms in excited and ground states, respectively. In equilibrium, T_s is given by [12,62]

$$T_s = \frac{T_\gamma + y_c T_b + y_{Ly\alpha} T_{Ly\alpha}}{1 + y_c + y_{Ly\alpha}}, \tag{4}$$

where y_c is the collisional coupling parameter, T_b is the baryon temperature, $y_{Ly\alpha}$ represents the Wouthuysen-Field effect [63,64] and $T_{Ly\alpha}$ is the Lyman-α ($Ly\alpha$) background temperature. The coefficients y_c and $y_{Ly\alpha}$ are given by $y_c = \frac{C_{10}T_*}{A_{10}T_b}$ and $y_{Ly\alpha} = \frac{P_{10}T_*}{A_{10}T_{Ly\alpha}}$ [65]. Here, C_{10} is the collisional deexcitation rate of the triplet hyperfine level, $P_{10} \approx 1.3 \times 10^{-12} S_\alpha J_{-21} s^{-1}$ is the indirect deexcitation rate due to Ly-α absorption, S_α is a factor of order unity that incorporates spectral distortions [66] and J_{-21} is the Lyman-α background intensity written in units of 10^{-21} erg cm^{-2} s^{-1} Hz^{-1} sr^{-1}, and can be estimated by the procedure mentioned in [12,67].

The baryon temperature T_b can be obtained from the standard evolution equations of T_b and x_e, the ionization fraction. The ionization fraction x_e is given by $x_e = n_e/n_H$, where n_e and n_H are the number densities of free electron and hydrogen, respectively, is an important quantity in estimating thermal evolution. Here, we will not consider exotic physics or nonstandard processes like dark matter decay. We just

consider standard evolution equations. These equations governing thermal evolution are given by [12,68,69]

$$(1+z)\frac{dT_b}{dz} = 2T_b + \frac{\Gamma_c}{H(z)}(T_b - T_\gamma), \tag{5}$$

$$(1+z)\frac{dx_e}{dz} = \frac{C_P}{H(z)}\left(n_H\alpha_B x_e^2 - 4(1-x_e)\beta_B e^{-\frac{3E_0}{4k_B T_\gamma}}\right), \tag{6}$$

where Γ_c ($\Gamma_c = \frac{8\sigma_T a_r T_\gamma^4 x_e}{3(1+f_{He}+x_e)m_e c}$) describes the Compton interaction rate (σ_T is the Thomson scattering cross section, a_r is the radiation constant, f_{He} is the fractional abundance of helium, m_e is the mass of an electron), C_P is the Peebles C factor [68,70], $E_0 = 13.6$ eV, k_B is the Boltzmann constant and α_B and β_B are the recombination and ionization coefficients, respectively. The Peebles C factor is given by [68]

$$C_P = \frac{\frac{3}{4}R_{Ly\alpha} + \frac{1}{4}\Lambda_{2s1s}}{\beta_B + \frac{3}{4}R_{Ly\alpha} + \frac{1}{4}\Lambda_{2s1s}}, \tag{7}$$

where $R_{Ly\alpha}$ represents the rate of escape of Ly α photons, $R_{Ly\alpha} = 8\pi H/(3n_H(1-x_e)\lambda_{Ly\alpha}^3)$, n_H is the total number density of hydrogen and $\Lambda_{2s,1s} \approx 8.22\ \mathrm{s}^{-1}$ [68]. α_B and β_B can be calculated using the procedure mentioned in [9,10]. Similar to the case of Eqs. (1) and (2), the cosmological dependence of the equations [Eqs. (5) and (6)] are enshrined in $H(z)$, the Hubble parameter.

III. BUCHERT'S BACKREACTION FORMALISM

Buchert's averaging procedure that we are using here is for the pressureless dust universe model [29,71]. Buchert's backreaction formalism simplifies the averaging problem by considering only scalar quantities to average. The spacetime is divided into flow-orthogonal hypersurfaces with the line element [29,37]

$$ds^2 = -dt^2 + g_{ij}dX^i dX^j, \tag{8}$$

where t is the proper time, X^i are Gaussian normal coordinates in the hypersurfaces and g_{ij} is the spatial three-metric of the hypersurfaces of constant t. The volume of a compact spatial domain $\mathcal{D}$ on these hypersurfaces is defined as

$$|\mathcal{D}|_g := \int_{\mathcal{D}} d\mu_g, \tag{9}$$

where $d\mu_g := \sqrt{{}^{(3)}g(t,X^1,X^2,X^3)}dX^1dX^2dX^3$. Now, we define a dimensionless ("effective") scale factor

$$a_{\mathcal{D}}(t) := \left(\frac{|\mathcal{D}|_g}{|\mathcal{D}_i|_g}\right)^{1/3}, \tag{10}$$

normalized by the volume of the initial domain $|\mathcal{D}_i|_g$, which can be considered the domain's volume at the present time, t_0. The average over a scalar quantity f is defined as

$$\langle f\rangle_{\mathcal{D}}(t) := \frac{\int_{\mathcal{D}} f(t,X^1,X^2,X^3)d\mu_g}{\int_{\mathcal{D}} d\mu_g}. \tag{11}$$

Using this averaging procedure and Einstein equations along with the continuity equation, Hamiltonian constraint, and Raychaudhuri equation gives us evolution equations,

$$3\frac{\ddot{a_{\mathcal{D}}}}{a_{\mathcal{D}}} = -4\pi G\langle\rho\rangle_{\mathcal{D}} + \mathcal{Q}_{\mathcal{D}}, \tag{12}$$

$$3H_{\mathcal{D}}^2 = 8\pi G\langle\rho\rangle_{\mathcal{D}} - \frac{1}{2}\langle\mathcal{R}\rangle_{\mathcal{D}} - \frac{1}{2}\mathcal{Q}_{\mathcal{D}}, \tag{13}$$

$$0 = \partial_t\langle\rho\rangle_{\mathcal{D}} + 3H_{\mathcal{D}}\langle\rho\rangle_{\mathcal{D}}, \tag{14}$$

where $\langle\rho\rangle_{\mathcal{D}}$, $\langle\mathcal{R}\rangle_{\mathcal{D}}$ and $H_{\mathcal{D}}$ are the averaged matter density, averaged spatial Ricci scalar and the Hubble parameter ($H_{\mathcal{D}} := \dot{a_{\mathcal{D}}}/a_{\mathcal{D}}$) of the domain $\mathcal{D}$, respectively. $\mathcal{Q}_{\mathcal{D}}$ is called the kinematical backreaction and is defined as

$$\mathcal{Q}_{\mathcal{D}} := \frac{2}{3}(\langle\theta^2\rangle_{\mathcal{D}} - \langle\theta\rangle_{\mathcal{D}}^2) - 2\langle\sigma^2\rangle_{\mathcal{D}}, \tag{15}$$

where θ is the local expansion rate and $\sigma^2 := 1/2\sigma_{ij}\sigma^{ij}$ is the squared rate of shear. The Hubble parameter $H_{\mathcal{D}}$ and $\langle\theta\rangle_{\mathcal{D}}$ are related by the relation $H_{\mathcal{D}} = 1/3\langle\theta\rangle_{\mathcal{D}}$. $\mathcal{Q}_{\mathcal{D}}$ is zero for a FLRW-like domain. The necessary condition of integrability connecting Eqs. (12) and (13) is given by

$$\frac{1}{a_{\mathcal{D}}^2}\partial_t(a_{\mathcal{D}}^2\langle\mathcal{R}\rangle_{\mathcal{D}}) + \frac{1}{a_{\mathcal{D}}^6}\partial_t(a_{\mathcal{D}}^6\mathcal{Q}_{\mathcal{D}}) = 0. \tag{16}$$

Equation (16) shows an important feature of the averaged equations as it couples the evolution of the averaged intrinsic curvature ($\langle\mathcal{R}\rangle_{\mathcal{D}}$) to the kinematical backreaction term ($\mathcal{Q}_{\mathcal{D}}$) that symbolizes the inclusion of matter inhomogeneities in the analysis. This relationship between $\langle\mathcal{R}\rangle_{\mathcal{D}}$ and $\mathcal{Q}_{\mathcal{D}}$ together with the term $\mathcal{Q}_{\mathcal{D}}$ embodies the diversion from homogeneity.

We now adopt a specific approach within the Buchert formalism, in which ensembles of disjoint regions represent the global domain [35–55]. Here, the global domain $\mathcal{D}$ is considered to be partitioned into subregions $\mathcal{F}_l$ that themselves consist of elementary space entities $\mathcal{F}_l^{(\alpha)}$. Therefore, mathematically, we have $\mathcal{D} = \cup_l \mathcal{F}_l$, where $\mathcal{F}_l := \cup_\alpha \mathcal{F}_l^{(\alpha)}$ and $\mathcal{F}_l^{(\alpha)} \cap \mathcal{F}_m^{(\beta)} = \varnothing$ for all $\alpha \neq \beta$ and $l \neq m$. The average of a scalar-valued function f on the domain $\mathcal{D}$ is given by

$$\begin{aligned}\langle f\rangle &:= |\mathcal{D}|_g^{-1}\int_{\mathcal{D}} f d\mu_g = \sum_l |\mathcal{D}|_g^{-1}\sum_\alpha \int_{\mathcal{F}_l^{(\alpha)}} f d\mu_g, \\ &= \sum_l \frac{|\mathcal{F}_l|_g}{|\mathcal{D}|_g}\langle f\rangle_{\mathcal{F}_l} = \sum_l \lambda_l\langle f\rangle_{\mathcal{F}_l},\end{aligned} \tag{17}$$

where

$$\lambda_l := \frac{|\mathcal{F}_l|_g}{|\mathcal{D}|_g} \tag{18}$$

is the volume fraction of the subregion $\mathcal{F}_l$ such that $\sum_l \lambda_l = 1$ and $\langle f \rangle_{\mathcal{F}_l}$ is the average of f on subregion $\mathcal{F}_l$. The scalar quantities ρ, $\mathcal{R}$, and $\mathcal{H}_\mathcal{D}$ are governed by Eq. (17), but $\mathcal{Q}_\mathcal{D}$, due to the presence of $\langle\theta\rangle^2_\mathcal{D}$ term, does not adhere to the above equation and instead follows

$$\mathcal{Q}_\mathcal{D} = \sum_l \lambda_l \mathcal{Q}_l + 3\sum_{l\neq m} \lambda_l \lambda_m (H_l - H_m)^2, \tag{19}$$

where $\mathcal{Q}_l$ and H_l are defined in subregion $\mathcal{F}_l$ in the same way as $\mathcal{Q}_\mathcal{D}$ and $H_\mathcal{D}$ are defined in the domain $\mathcal{D}$.

We can also define the scale factor a_l for a subregion $\mathcal{F}_l$. By definition, the different subregions are disjoint; therefore it follows that $|\mathcal{D}|_g = \sum_l |\mathcal{F}_l|_g$ and hence, using Eq. (10), we have

$$a^3_\mathcal{D} = \sum_l \lambda_{l_i} a^3_l, \tag{20}$$

where $\lambda_{l_i} = \frac{|\mathcal{F}_{l_i}|_g}{|\mathcal{D}_i|_g}$ is the initial volume fraction which can also be taken as the volume fraction at present and can be represented as λ_{l_0}, where the subscript 0 stands for quantities calculated at the present time. Differentiating this relation twice with respect to the foliation time results in

$$\frac{\ddot{a}_\mathcal{D}}{a_\mathcal{D}} = \sum_l \lambda_l \frac{\ddot{a}_l(t)}{a_l(t)} + \sum_{l\neq m} \lambda_l \lambda_m (H_l - H_m)^2. \tag{21}$$

IV. A MODEL OF MULTIPLE SUBREGIONS

Several studies have been performed within the Buchert averaging scheme using models having just one type of overdense subdomain and one type of underdense subdomain [42,43,45–48]. This oversimplifies the actual spacetime scenario with matter inhomogeneities where the matter density may vary from very low to very high across different subdomains. Therefore, a more realistic model would have multiple overdense and underdense subregions with distinct evolution profiles. A similar model has been used in [54] to study the future evolution of the currently accelerating Universe with multiple inhomogeneous domains.

Here, using Buchert's backreaction framework, we consider a model of the Universe in which domain $\mathcal{D}$ comprises multiple underdense and overdense subregions, viz., there are i number of overdense subregions and i number of underdense subregions. The underdense subregions have densities smaller than those of the overdense subregions. Our underdense subregions are modelled to mimic almost empty FLRW regions with very little matter (dust) present. The overdense subregions are modeled to mimic FLRW models with matter (dust) content. The underdense subregions are taken to have Friedmann-like $1/a^2$ negative curvature, while the overdense subregions have Friedmann-like $1/a^2$ positive curvature. The time evolution of the scale factor of ith overdense subregions, a_{o_i}, is given in terms of a development angle ϕ_{o_i} of the ith overdense subregion [72],

$$a_{o_i} = \frac{q_{o_{i,0}}}{2q_{o_{i,0}} - 1}(1 - \cos\phi_{o_i}), \tag{22}$$

$$t = t_0 \frac{(\phi_{o_i} - \sin\phi_{o_i})}{(\phi_{o_{i,0}} - \sin\phi_{o_{i,0}})}, \tag{23}$$

where $q_{o_{i,0}}$ and $\phi_{o_{i,0}}$ are, respectively, the deceleration parameter of the ith overdense subregion and the value of ϕ_{o_i} at time t_0, which is the present time. $q_{o_{i,0}}$ should be greater than $1/2$ [72]. Here, we have taken $q_{o_{i,0}}$ to have a range of values from $1/2$ to 1. The time t in Eq. (23) [41,55] is the cosmic time, although for each overdense subregion, this t is parametrized in terms of $(\phi_{o_{i,0}}, \phi_{o_i})$ ($\phi_{o_{i,0}}$ itself is a function of $q_{o_{i,0}}$). The value of t_0 is the same across all overdense subregions as well as for the global domain which is ensured by the specific form of Eq. (23). The time evolution of the scale factor of ith underdense subregions, a_{u_i} is given in terms of a development angle ϕ_{u_i} of the ith underdense subregion [72],

$$a_{u_i} = \frac{q_{u_{i,0}}}{1 - 2q_{u_{i,0}}}(\cosh\phi_{u_i} - 1), \tag{24}$$

$$t = t_0 \frac{(\sinh\phi_{u_i} - \phi_{u_i})}{(\sinh\phi_{u_{i,0}} - \phi_{u_{i,0}})}, \tag{25}$$

where $q_{u_{i,0}}$ and $\phi_{u_{i,0}}$ are, respectively, the deceleration parameter of the ith underdense subregion and the value of ϕ_{u_i} at time t_0, which is the present time. $q_{u_{i,0}}$ has a range of values from 0 to $1/2$ [72]. The time t in Eq. (25) is the cosmic time, although for each underdense subregion, this t is parametrized in terms of $(\phi_{u_{i,0}}, \phi_{u_i})$ ($\phi_{u_{i,0}}$ itself is a function of $q_{u_{i,0}}$). The value of t_0 is the same across all underdense and overdense subregions as well as for the global domain, which is ensured by the specific form of Eqs. (23) and (25). Since the values of t_0 and $H_{\mathcal{D}_0}$ are interrelated, one needs to fix either of them [55]. In our subsequent analysis, we choose $H_{\mathcal{D}_0}$ to be 70 $\mathrm{km\,s^{-1}\,Mpc^{-1}}$. The value of t_0 is calculated using the procedure used in [55], modified for our model (see Appendix A).

Note that a_{o_i} and a_{u_i} can be expressed in terms of the volume of the respective subregions using Eq. (10), which gives us

$$a_{o_i}(t) \coloneqq \left(\frac{|\mathcal{D}|_{o_i}}{|\mathcal{D}_0|_{o_i}}\right)^{1/3}, \qquad a_{u_i}(t) \coloneqq \left(\frac{|\mathcal{D}|_{u_i}}{|\mathcal{D}_0|_{u_i}}\right)^{1/3}, \tag{26}$$

where $|\mathcal{D}|_{o_i}$ is the volume of the ith overdense subregions at time t, $|\mathcal{D}_0|_{o_i}$ is the volume of the ith overdense subregion at time t_0 as was done in Eq. (10), and similarly for the case of the underdense subregions. Equations (10) and (26) require that at $t = t_0$, $a_{\mathcal{D}} = a_{o_i} = a_{u_i} = 1$, leading to

$$\cos\phi_{o_{i,0}} = \left(\frac{1}{q_{o_{i,0}}} - 1\right), \quad \cosh\phi_{u_{i,0}} = \left(\frac{1}{q_{u_{i,0}}} - 1\right). \tag{27}$$

For a given value of $q_{o_{i,0}}$ and $q_{o_{i,0}}$; $a_{o_i}(t)$ and $a_{u_i}(t)$ can be calculated using Eqs. (22)–(25) and (27). Then using Eq. (20), $a_{\mathcal{D}}(t)$ can be obtained provided λ_{l_0}, which is the set of all $\lambda_{u_i,0}$ and $\lambda_{o_i,0}$, is known.

It may be noted that $a_{\mathcal{D}}$ can also be obtained from solving the second order differential equation [Eq. (21)]. Using Eqs. (22) and (24) in Eq. (21), we get

$$\frac{\ddot{a}_{\mathcal{D}}}{a_{\mathcal{D}}} = \left(\sum_i \lambda_{o_i}\frac{\ddot{a}_{o_i}}{a_{o_i}}\right) + \left(\sum_j \lambda_{u_j}\frac{\ddot{a}_{u_i}}{a_{u_i}}\right) + \left(\sum_k\sum_l \lambda_k\lambda_l(H_l - H_k)^2\right), \tag{28}$$

where λ_{o_i} is the volume fraction of the ith overdense subregion, λ_{u_j} is the volume fraction of the jth underdense subregion, λ is the set of all λ_{o_i} and λ_{u_i} and H is, respectively, the set of all H_{o_i} and H_{u_i}. The combined volume fraction of all the underdense subregions is given by λ_u, i.e., $\sum_i \lambda_{u_i} = \lambda_u$. Similarly, the total volume fraction of all the overdense subregions is given by $\sum_i \lambda_{o_i} = \lambda_o$. Clearly, $\lambda_o + \lambda_u = 1$. The evaluation of $a_{\mathcal{D}}$ obtained from these two methods is identical, as confirmed through our analysis.

The volume fraction of the ith overdense subregion can be written as

$$\lambda_{o_i} = \frac{|\mathcal{F}_{o_i}|_g}{|\mathcal{D}|_g} = \frac{a_{o_i}^3|\mathcal{F}_{o_i,0}|_g}{a_{\mathcal{D}}^3|\mathcal{D}_0|_g} = \lambda_{o_i,0}\frac{a_{o_i}^3}{a_{\mathcal{D}}^3}, \tag{29}$$

where t_0 is a reference time which can be taken as the present time, $|\mathcal{F}_{o_i}|_g$ is the volume of the ith overdense subregion, $|\mathcal{F}_{o_i,0}|_g$ is the volume of the ith overdense subregion at time t_0, $|\mathcal{D}_0|_g$ is the volume of the domain $\mathcal{D}$ at time t_0 and $\lambda_{o_i,0}$ is the volume fraction of the ith overdense subregion at time t_0. The present time (t_0) value of (λ_o, λ_u) is given by $(\lambda_{o,0}, \lambda_{u,0})$, which we have taken to be (0.09,0.91) [37].

In our model, we consider the present time volume fraction of ith underdense subregion, $\lambda_{u_i,0}$ to have a Gaussian distribution within the allowed range of $q_{u_{i,0}}$ from 0 to 1/2, given by

$$\lambda_{u_i,0} = \frac{N_u}{\sigma_u\sqrt{2\pi}}e^{-(q_{u_{i,0}}-\mu_u)^2/2\sigma_u^2}, \tag{30}$$

where N_u is a normalization constant, which ensures that $\sum_i \lambda_{u_i,0} = \lambda_{u,0} = 0.91$, μ_u is the mean value of $q_{u_{i,0}}$ and σ_u is the standard deviation of $q_{u_{i,0}}$. Therefore, each ith underdense subregion is associated with a particular value of $q_{u_{i,0}}$ and $\lambda_{u_i,0}$ such that $q_{u_{i,0}}$ varies from 0 to 1/2 in the i number of underdense subregions and $\sum_i \lambda_{u_i,0} = 0.91$.

The present-time volume fraction of ith overdense subregion, $\lambda_{o_i,0}$ is considered to have a Gaussian profile within the allowed range of $q_{o_{i,0}}$ from 1/2 to 1 given by

$$\lambda_{o_i,0} = \frac{N_o}{\sigma_o\sqrt{2\pi}}e^{-(q_{o_{i,0}}-\mu_o)^2/2\sigma_o^2}, \tag{31}$$

where N_o is a normalization constant that ensures that $\sum_i \lambda_{o_i,0} = \lambda_{u,0} = 0.09$, μ_o is the mean value of $q_{o_{i,0}}$ and σ_o is the standard deviation of $q_{o_{i,0}}$. In this case, each ith overdense subregion is associated with a particular value of $q_{o_{i,0}}$ and $\lambda_{o_i,0}$, where $q_{o_{i,0}}$ lies within the range 1/2 to 1 across the i number of overdense subregions and $\sum_i \lambda_{o_i,0} = 0.09$. The volume fraction of the ith underdense subregion at a time t, λ_{u_i} is related to the volume fraction at present time t_0 by

$$\lambda_{u_i} = \lambda_{u_i,0}\left(\frac{1-\sum_i\lambda_{o_i}}{1-\sum_i\lambda_{o_i,0}}\right). \tag{32}$$

We have used the Gaussian distribution to define the present time volume fraction of various subregions. The actual physical distribution can only be known by extensive galactic surveys of the matter distribution in the Universe. Although some such surveys have been performed for the local Universe, for the redshifts of our interest, no such surveys exist. Without such surveys, we assume a normal distribution used in analysis where we do not expect any bias. The Gaussian distribution is well known and extensively used in diverse physical analyses to model unbiased physical conditions. (Further details of our model are provided in Appendix B.)

Using Eq. (19), the kinematical backreaction term for the domain $\mathcal{D}$ for our model effectively becomes

$$\mathcal{Q}_{\mathcal{D}} = \sum_i \lambda_{o_i}\mathcal{Q}_{o_i} + \sum_j \lambda_{u_j}\mathcal{Q}_{u_j} + 3\sum_{l\neq m}\lambda_l\lambda_m(H_l - H_m)^2, \tag{33}$$

where $\mathcal{Q}_{o_i}$ is the kinematical backreaction term for the ith overdense subregion, $\mathcal{Q}_{u_i}$ is for the ith underdense subregion. The summation in the last term runs over the

sets of all λ_{o_i}, λ_{u_i}, H_{o_i}, and H_{u_i}. Equation (16) couples the kinematical backreaction term to the Ricci scalar, and our subregions are also governed by this coupling. Therefore, by selectively choosing the curvatures of our subregions, we can make the respective kinematical backreaction terms for these subregions equal to zero [37,73]. Hence, in this case, the global kinematical backreaction is governed by only the interplay of the subdomain Hubble evolutions and volume fractions [third term of Eq. (33)]. Note that the above assumptions are made in the context of our present model. On the other hand, if the subdomains are endowed with dynamical curvature, other intricate effects could arise through kinematical backreaction, as may also happen in a more general case where the subregions may not necessarily be FLRW.

Obtaining the values of $\lambda_{o_i,0}$ and $\lambda_{u_i,0}$ from Eqs. (30) and (31), respectively, and using these in Eqs. (29) and (32) gives us λ_{o_i} and λ_{u_i}. Hubble parameters for the subregions can be obtained from Eqs. (22), (23) and Eqs. (24), (25). We can then use Eq. (28) to get $a_{\mathcal{D}}(t)$ and $H_{\mathcal{D}}(t)$. We next relate these quantities calculated theoretically from our model with observational quantities redshift and angular diameter distance by using the covariant scheme [56,57], given by

$$1+z=\frac{1}{a_{\mathcal{D}}}, \tag{34}$$

$$H_{\mathcal{D}}\frac{d}{dz}\left((1+z)^2 H_{\mathcal{D}}\frac{dD_A}{dz}\right)=-4\pi G\langle\rho\rangle_{\mathcal{D}} D_A. \tag{35}$$

Equation (34) relates $a_{\mathcal{D}}(t)$ with the cosmological redshift $z(t)$ and Eq. (35) relates the angular diameter distance D_A with $\langle\rho\rangle_{\mathcal{D}}$ and $H_{\mathcal{D}}$. Here, we use Eq. (34) to obtain $z(t)$ from $a_{\mathcal{D}}(t)$. We can thus evaluate $H_{\mathcal{D}}(z)$ using $H_{\mathcal{D}}(t)$ [from Eq. (28)] and $z(t)$ [from Eq. (34)].

In Fig. 1(a), $H_{\mathcal{D}}(z)/H_{\mathcal{D},0}$ has been plotted as a function of redshift z for different values of n, the number of each type of subregion—overdense and underdense. The total subregions are $2n$, n, overdense subregions and n underdense subregions. Here, $H_{\mathcal{D},0}$ is the value of $H_{\mathcal{D}}(z)$ at $z=0$. Depending on the model parameters, our backreaction model may be very close to a perturbed FRW or mimic a single FRW at very early times. Considering a very high value of n does not lead to a significant difference, as can be seen in our following analysis. We define

$$\langle H_{\mathcal{D}_n}\rangle=\frac{1}{\sum i}\sum_i\left|\frac{(H_{\mathcal{D}}(z)/H_{\mathcal{D},0})|_{500}-(H_{\mathcal{D}}(z)/H_{\mathcal{D},0})|_n}{(H_{\mathcal{D}}(z)/H_{\mathcal{D},0})|_{500}}\right|_{z=z_i}, \tag{36}$$

which denotes the redshift-averaged variation of $H_{\mathcal{D}_n}$, from the limiting case of $n=500$. In this analysis, we split the redshift range (i.e., $0\le z\le 100$) into 100 bins. In Eq. (36), i is the index number of such bins. The variation of $\langle H_{\mathcal{D}_n}\rangle$ with n are plotted in Fig. 1(b). In this figure, the plots are for different chosen sets of μ_o and μ_u, while the other two parameters are kept at $\sigma_u=0.01$ and $\sigma_o=0.01$. For $n\ge 100$, the average fluctuation is less than $\sim 10^{-6}$. Given the above results, we chose $n=100$ for our remaining calculations.

From here onwards, in our calculations, we consider one hundred underdense and one hundred overdense subdomains. These subdomains are characterized by the respective volume fractions, λ_{o_i} and λ_{u_i} [Eqs. (29) and (32)],

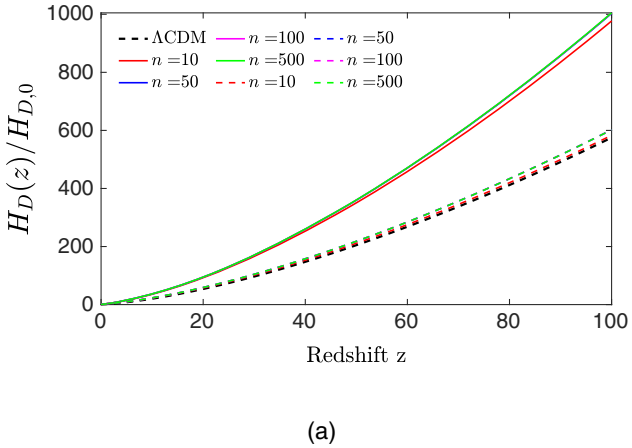

(a)

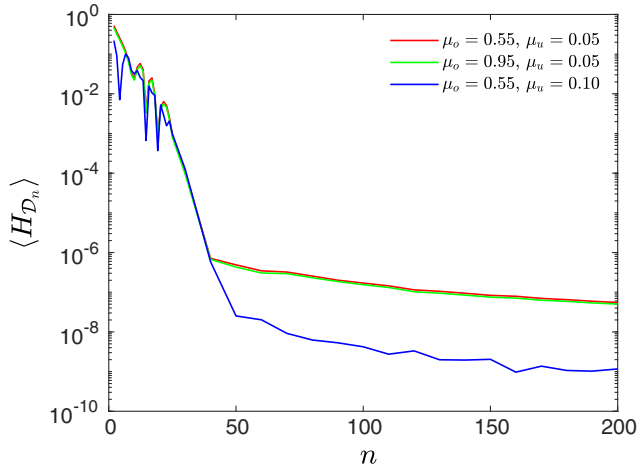

(b)

FIG. 1. Subplot (a) is the plot of $H_{\mathcal{D}}(z)/H_{\mathcal{D},0}$ for our backreaction model for different values of n, the number of underdense and overdense subregions. Here, $H_{\mathcal{D},0}$ is the value of $H_{\mathcal{D}}(z)$ at $z=0$. The values of our model parameters are chosen as follows: $\mu_u=0.49$, $\sigma_u=0.01$, $\mu_o=0.51$, and $\sigma_o=0.01$ for solid lines and $\mu_u=0.15$, $\sigma_u=0.01$, $\mu_o=0.51$, and $\sigma_o=0.01$ for dashed lines. The ΛCDM model curve is shown with a black dashed line. Subplot (b) is the plot of $\langle H_{\mathcal{D}_n}\rangle$ versus n, the total number of subregions of each type. We take $\sigma_u=\sigma_o=0.01$ for all three lines, while μ_u and μ_o are varied as mentioned in the legend.

distributed using a Gaussian profile among these subdomains [Eqs. (30) and (31)]. Our underdense regions are characterized by parameters $q_{u_{i,0}}$ that vary from $0 < q_{u_{i,0}} < 0.5$ [72]. This range for $q_{u_{i,0}}$ has been taken to ensure a wide range of underdense subregions is present in our model to mimic a variety of underdense regions that may be present in the Universe. μ_u and σ_u are the mean and standard deviation of the Gaussian profile of the underdense regions. The underdense subregion with $q_{u_{i,0}} = \mu_u$ will have the largest value of λ_{u_i} and thus will be the most prominent underdense subregion in the analysis. Here, σ_u governs the distribution width about a given μ_u. Similarly, our overdense regions are characterized by parameters $q_{o_{i,0}}$ varying from $1/2 < q_{o_{i,0}} < 1$. This range for $q_{o_{i,0}}$ has been taken to ensure that a wide range of overdense subregions is present in our model to mimic a variety of overdense regions that may be present in the Universe. μ_o and σ_o are the mean and standard deviation for the Gaussian profile of overdense regions. The overdense subregion with $q_{o_{i,0}} = \mu_o$ will have the highest value of λ_{o_i} and, therefore, will be the most prominent overdense subregion in the analysis. σ_o is the standard deviation of the distribution, which governs the width of the distribution about the mean value.

In Fig. 2, the average density parameters are plotted as a function of the redshift in the redshift range ($z < 30$). See Appendix B for the calculation of these average density parameters. The density parameter associated with kinematical backreaction $\mathcal{Q}_\mathcal{D}$ plays a significant role in our backreaction model at late redshifts (around $z = 5$, as seen from the inset), embodying the departure from FLRW behavior in our framework. The $\mathcal{Q}_\mathcal{D}$ term becomes negligible at large redshifts, which can be seen from the corresponding plot in Fig. 2. The term $\Omega_\mathcal{Q}^\mathcal{D}$ going to zero at high redshifts (or at early times) shows that our model can mimic a perturbed FLRW model at early times.

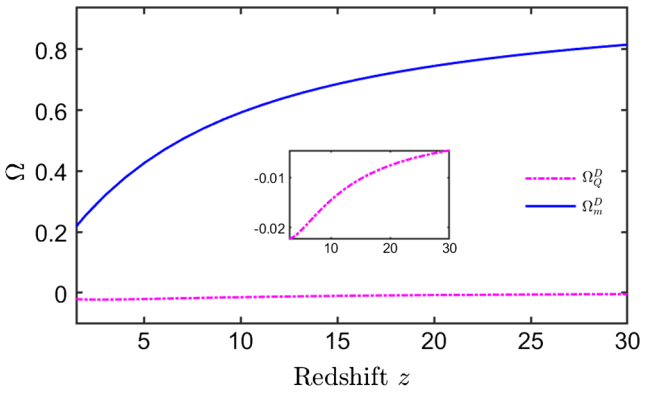

FIG. 2. Plot of average density parameters, $\Omega_m^\mathcal{D}$ and $\Omega_\mathcal{Q}^\mathcal{D}$ as a function of redshift, z. The values of the parameters are chosen as $\mu_u = 0.01$, $\sigma_u = 0.01$, $\mu_o = 0.99$, and $\sigma_o = 0.01$. The inset shows the magnified plot for $\Omega_\mathcal{Q}^\mathcal{D}$, the density parameter for kinematical backreaction term $\mathcal{Q}_\mathcal{D}$.

In Fig. 3, the variation with respect to the redshift of $H_\mathcal{D}(z)/H_{\mathcal{D},0}$ [here $H_{\mathcal{D},0}$ is the value of $H_\mathcal{D}(z)$ at $z = 0$] for our backreaction model and for the ΛCDM model [$H(z)/H_0$ for ΛCDM, $H_0 = H(z = 0)$] are plotted. Our backreaction model has four parameters that can be varied: $\mu_u, \sigma_u, \mu_o, \sigma_o$. One of the above parameters is varied in the four subfigures while keeping the other three fixed. From Fig. 3(a), it can be observed that larger values of parameter μ_o result in larger values of the quantity $H_\mathcal{D}(z)/H_{\mathcal{D},0}$, although the variation is very less and from Fig. 3(c) it can be observed that larger values of parameter μ_u result in larger values of the quantity $H_\mathcal{D}(z)/H_{\mathcal{D},0}$. Let us first consider Fig. 3(c) where μ_u is being varied, keeping the other three parameters fixed. Since μ_u is the mean of the Gaussian distribution of $\lambda_{u_i,0}$, it corresponds to the subregion with the largest value of $\lambda_{u_i,0}$ in the distribution. The subregion with $q_{u_{i,0}} = \mu_u$ possesses the largest value of $\lambda_{u_i,0}$ and, therefore, the largest value of λ_{u_i} also, from Eq. (32). It follows from Eq. (17) that this underdense subregion through its H_{u_i} provides the largest contribution among all other underdense subregions in the determination of H_u, the total Hubble parameter for all the underdense subregions combined, and consequently, provides the largest contribution in $H_\mathcal{D}$ among all other underdense subregions. Therefore, in Fig. 3(c) with all other parameters fixed, the plotlines for $H_\mathcal{D}$ follow the trend of variation of H_{u_i} with respect to the redshift z, of the subregion with $q_{u_{i,0}} = \mu_u$. The higher values of $q_{u_{i,0}}$ result in higher values of $H_u(z)$ at higher values of z, which is observed in Fig. 3(c), where higher values of μ_u give higher values of $H_\mathcal{D}(z)/H_{\mathcal{D},0}$. The behavior of the plotlines in Fig. 3(a) can also be explained similarly, where the corresponding underdense subregion analysis replaces the overdense subregion analysis. In Fig. 3(a), there is not much difference between the plotlines. This can be ascertained to the fact that overdense subregions have less impact on the global domain dynamics. The reason for this is that the collective volume fraction of the overdense subregions is much smaller than the collective volume fraction of the underdense subregions.

On the other hand, from the Figs. 3(b) and 3(d), it can be seen that larger values of σ_o and σ_u lead to larger values of the quantity $H_\mathcal{D}(z)/H_{\mathcal{D},0}$. Note that σ_o and σ_u represent the spread of the Gaussian distributions. In Figs. 3(b) and 3(d), only σ_o and σ_u are varied, respectively, keeping the other three parameters fixed. Therefore, a wider distribution with the same mean is considered in Figs. 3(b) and 3(d). A wider distribution results in more subregions becoming significant than for a narrower distribution. As the contributions of more subregions become effective, the values of the combined Hubble parameters for the overdense and underdense subregions, H_o and H_u, respectively, increase, and hence the value of $H_\mathcal{D}$ also increases, which is observed in Figs. 3(b) and 3(d). Similar to the case of Fig. 3(a), varying σ_o in Fig. 3(b) does not have much effect on the plotlines.

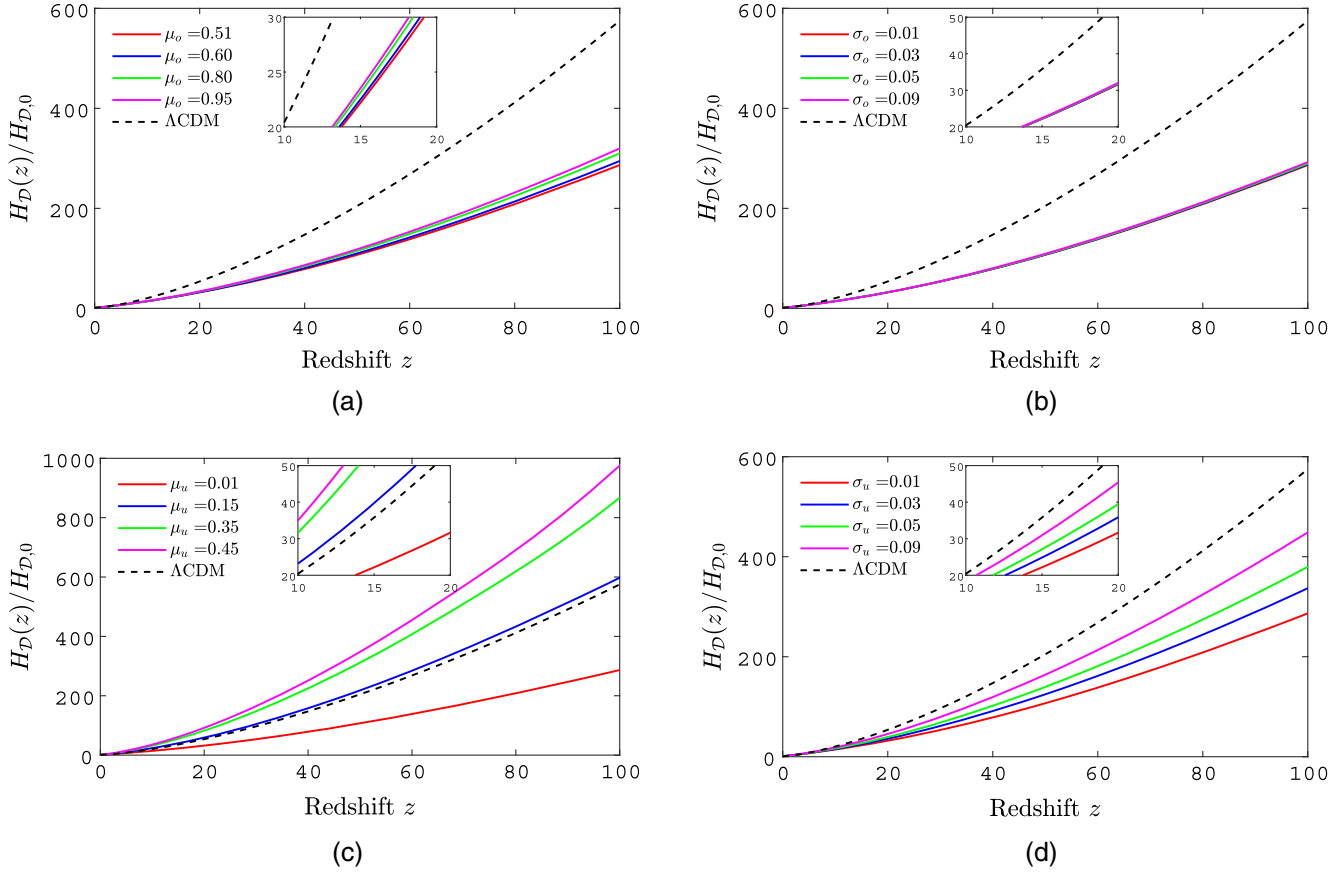

FIG. 3. Plots of $H_{\mathcal{D}}(z)/H_{\mathcal{D},0}$ for ΛCDM and our backreaction model as a function of z. Our backreaction model has four parameters that can be varied: μ_u, σ_u, μ_o, σ_o. In (a) μ_o is varied with $\sigma_o = \sigma_u = 0.01$ and $\mu_u = 0.01$ fixed. In (b) σ_o is varied with $\mu_o = 0.51$, $\sigma_u = 0.01$, and $\mu_u = 0.01$ fixed. In (c) μ_u is varied with $\sigma_o = \sigma_u = 0.01$ and $\mu_o = 0.51$ fixed. In (d) σ_u is varied with $\sigma_o = 0.01$, $\mu_o = 0.51$ and $\mu_u = 0.01$ fixed. The insets show the plot lines for the redshift range 10–20. The value of H_0 (Hubble parameter at the present time) used is 100 $h\,\mathrm{km\,s^{-1}\,Mpc^{-1}}$ where $h = 0.7$.

Therefore, model parameters associated with the overdense subregions do not have significant impact on the global domain dynamics.

V. EFFECT OF INHOMOGENEITIES ON THE 21-CM BRIGHTNESS TEMPERATURE

To analyze the brightness temperature of the 21-cm signal in the context of our model of multiple subregions of spacetime with matter distribution inhomogeneities, we replace $H(z)$ in the equations of 21-cm cosmology with $H_{\mathcal{D}}(z)$ (Fig. 3), which is the effective Hubble parameter calculated from our model using Eq. (28). Here, we employ the general scheme to calculate the 21-cm brightness temperature T_{21} for both ΛCDM and our backreaction model. The only difference between these two models is calculating the Hubble parameter $H(z)$, where z is the redshift. For the ΛCDM model, $H(z)$ is calculated using the standard relation of the Hubble parameter with various density parameters, Ωs. In contrast, for our model $H(z)$ is replaced by $H_{\mathcal{D}}(z)$, since we are interested in the evaluation of all physical quantities with respect to the global domain.

From Eq. (1), using Taylor expansion of $e^{-\tau(z)}$, and ignoring higher order terms of $\tau(z)$, we get

$$T_{21} \approx \frac{T_s - T_\gamma}{1+z}\tau(z).$$

Now, from Eq. (2), for $\delta_r v_r = 0$, $\tau(z) \propto 1/H(z)$. Therefore,

$$T_{21} \propto \frac{T_s - T_\gamma}{1+z}\frac{1}{H(z)}. \tag{37}$$

Thus, for a given value of T_s and T_γ, T_{21} is inversely proportional to $H(z)$. Note that the sign of T_{21} is governed by T_s and T_γ. If $T_s > T_\gamma$, then T_{21} is positive and negative for vice versa. $H(z)$ has effect only on the magnitude of T_{21}. Also note that T_{21} is related to $H(z)$ via T_s, which itself depends on $H(z)$ [from Eqs. (4) and (5)], but the dominant and more direct relationship between T_{21} and $H(z)$ is from Eq. (37).

Though the primary redshift range of interest for our present analysis is $14 < z < 20$ corresponding to the range

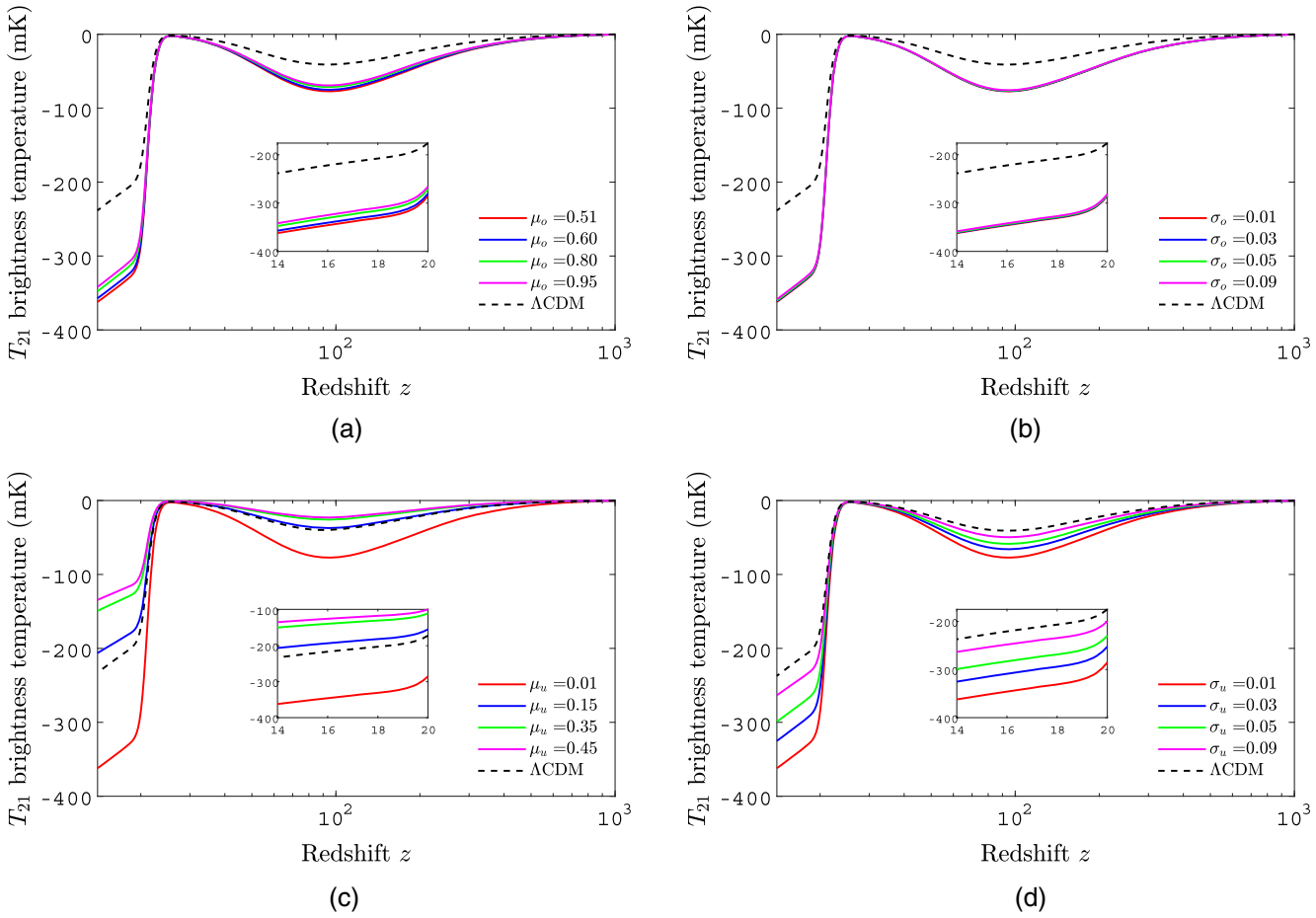

FIG. 4. Plots of brightness temperature T_{21} for the ΛCDM model and our backreaction model for the redshift range 14–1000. Our backreaction model has four parameters that can be varied: $\mu_u, \sigma_u, \mu_o, \sigma_o$. In (a) μ_o is varied with $\sigma_o = \sigma_u = 0.01$ and $\mu_u = 0.01$ fixed. In (b) σ_o is varied with $\mu_o = 0.51$, $\sigma_u = 0.01$, and $\mu_u = 0.01$ fixed. In (c) μ_u is varied with $\sigma_o = \sigma_u = 0.01$ and $\mu_o = 0.51$ fixed. In (d) σ_u is varied with $\sigma_o = 0.01$, $\mu_o = 0.51$, and $\mu_u = 0.01$ fixed. The value of H_0 (Hubble parameter at the present time) used is $100\ h\,\mathrm{km\,s^{-1}\,Mpc^{-1}}$ where $h = 0.7$. The insets show the plot lines in the redshift range of our interest.

of the EDGES result [6], there are various future proposed experiments to analyze the 21 cm signal at various redshift ranges [74–78]. In Fig. 4, we display results for a large redshift range up to $z = 1000$, given the above-proposed observations. The current analysis focuses on a much narrower regime of $14 < z < 20$ as displayed in the figure insets.

In Fig. 4, the variations of the brightness temperature T_{21} in mK as a function of redshift z using Eq. (1) in the redshift range 14–1000 are plotted for both the ΛCDM model and our backreaction model. In the case of our model, $H(z)$ is replaced by $H_{\mathcal{D}}(z)$ (plotted in Fig. 3). Our backreaction model has four parameters that can be varied: $\mu_u, \sigma_u, \mu_o, \sigma_o$. One of the parameters varied in each of the four subfigures, while the other three were fixed. Each subplot of Fig. 4 has a relation with the corresponding subplot of Fig. 3 via Eq. (37). In Fig. 3(c), lower values of μ_u yielded lower values of $H_{\mathcal{D}}(z)$, and since $H_{\mathcal{D}}(z)$ is inversely proportional to the magnitude of T_{21}, lower values of μ_u should give us the greater magnitude of T_{21}. This is what is observed in Fig. 4(c). Other subplots of Fig. 4 also have a one-to-one correspondence with their counterparts in Fig. 3, which can be explained similarly. At lower values of the redshift z, our backreaction model for a large range of parameters leads to lower brightness temperature than the ΛCDM model. In general, lower values of μ_o, μ_u, σ_o, and σ_u lead to lower (more negative) values of T_{21}.

In Fig. 5, the variation of T_{21} at $z = 17.2$ in the μ_o-σ_o plane is shown for different sets of values of (μ_u, σ_u) using a contour plot. The value of μ_o varies in the range of 0.5–1.0 along the x axis, while σ_o is varied in the range 0.01–0.09 along the y axis. The contour colors describe the value of $T_{21}(z = 17.2)$ per the color bar at the bottom of the figure. In Figs. 5(a) and 5(b), (μ_u, σ_u) are (0.01, 0.01) and (0.01, 0.09), respectively. Figure 5(a) has a lower value (more negative) of $T_{21}(z = 17.2)$ compared to Fig. 5(b). There is also very little variation within the individual Figs. 5(a) and 5(b). This shows that fixing (μ_u, σ_u) and varying (μ_o, σ_o) has very little effect on the calculation of T_{21} at $z = 17.2$. However, changing σ_u between Figs. 5(a)

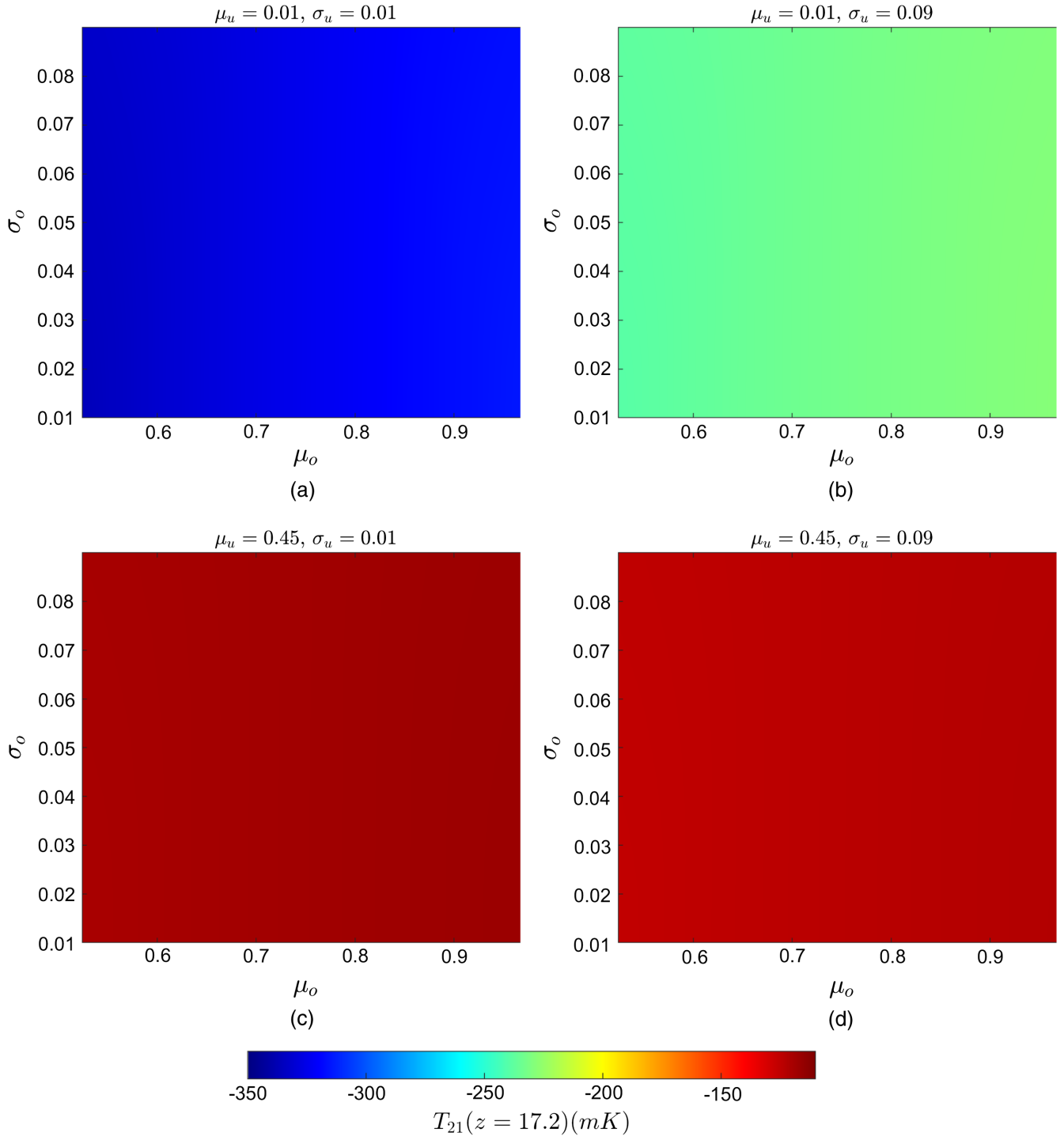

FIG. 5. Contour representation of $T_{21}(z = 17.2)(mK)$ in the σ_o-μ_o plane for (a) $\mu_u = 0.01$, $\sigma_u = 0.01$, (b) $\mu_u = 0.01$, $\sigma_o = 0.09$, (c) $\mu_u = 0.45$, $\sigma_u = 0.01$, (d) $\mu_u = 0.45$, $\sigma_u = 0.09$.

and 5(b) results in significant variation. This also shows the insignificance of the model parameters associated with overdense subregions in the dynamics of the global domain. From Figs. 5(c) and 5(d), it can be seen that $T_{21}(z = 17.2)$ has high values (from -150 to -110 mK) for $(\mu_u, \sigma_u) = (0.45, 0.01)$ and $(0.45,\ 0.09)$. Changing σ_u from 0.01 to 0.09 while keeping μ_u fixed in Figs. 5(c) and 5(d) has little effect on the value of $T_{21}(z = 17.2)$. In these subplots, $T_{21}(z = 17.2)$ has the lowest value of around -350 mK in the lower left portion of Fig. 5(a). This affirms our analysis of Fig. 4 that lower values of σ_u, σ_o, μ_o, and μ_u lead to lower values (more negative) of $T_{21}(z = 17.2)$. From Figs. 5(a) and 5(c), it can be seen that changing the value of μ_u keeping σ_u fixed has a more

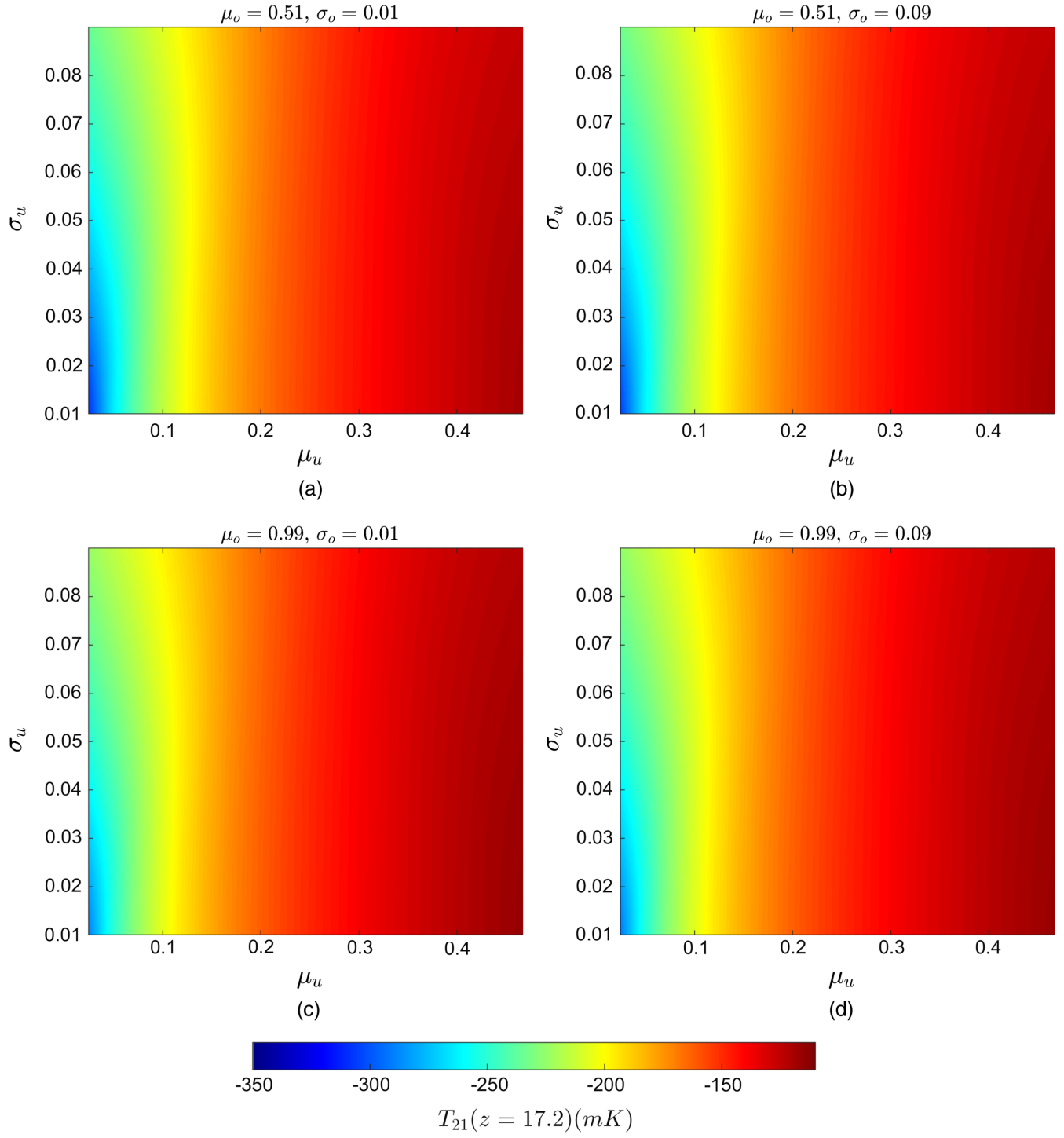

FIG. 6. Contour representation of $T_{21}(z = 17.2)$ (mK) in the σ_u-μ_u plane for (a) $\mu_o = 0.51$, $\sigma_o = 0.01$, (b) $\mu_o = 0.51$, $\sigma_o = 0.09$, (c) $\mu_o = 0.99$, $\sigma_o = 0.01$, (d) $\mu_o = 0.99$, $\sigma_o = 0.09$.

prominent effect on the brightness temperature than doing vice versa.

In Fig. 6, the variation of T_{21} at $z = 17.2$ in the μ_u-σ_u plane is shown for different sets of values of (μ_o, σ_o) using a contour plot. The value of μ_u varies in the range of 0–0.5 along the x axis while σ_u is varied along the y axis in the range of 0.01–0.09. In Figs. 6(a) and 6(b), μ_o is fixed at 0.51, and σ_o has the values of 0.01 and 0.09, respectively. In Figs. 6(c) and 6(d), μ_o is fixed at 0.99 while σ_u has the values of 0.01 and 0.09, respectively. The effect of varying σ_o while keeping μ_o fixed can also be seen from these two subplots. From Figs. 6(a) and 6(c), it can be seen that

changing the value of μ_o keeping σ_o fixed has a slightly more prominent effect on the brightness temperature than vice versa. The lowest value of $T_{21}(z = 17.2)$ of around -320 mK is obtained in the bottom left part of the Fig. 5(a) of the figure for $\mu_u \approx 0.01$. This also affirms our analysis of Fig. 4 that lower values of σ_u, σ_o, μ_o, and μ_u lead to lower values (more negative) of $T_{21}(z = 17.2)$. This figure also highlights the insignificance of overdense parameters as all four subplots are very much alike, so changing the overdense parameters does not affect the output much.

VI. OBSERVATIONAL CONSTRAINTS

We now examine the backreaction framework in the context of our model of multiple subregions with respect to observational data and determine the optimum values of our model parameters. We perform a Bayesian analysis to compare our model with the Union 2.1 supernova Ia distance modulus versus redshift data [79]. To compare our model with the observational data, we employ the earlier-mentioned covariant scheme [Eqs. (34) and (35)]. The first equation of the covariant scheme [Eq. (34)] relates

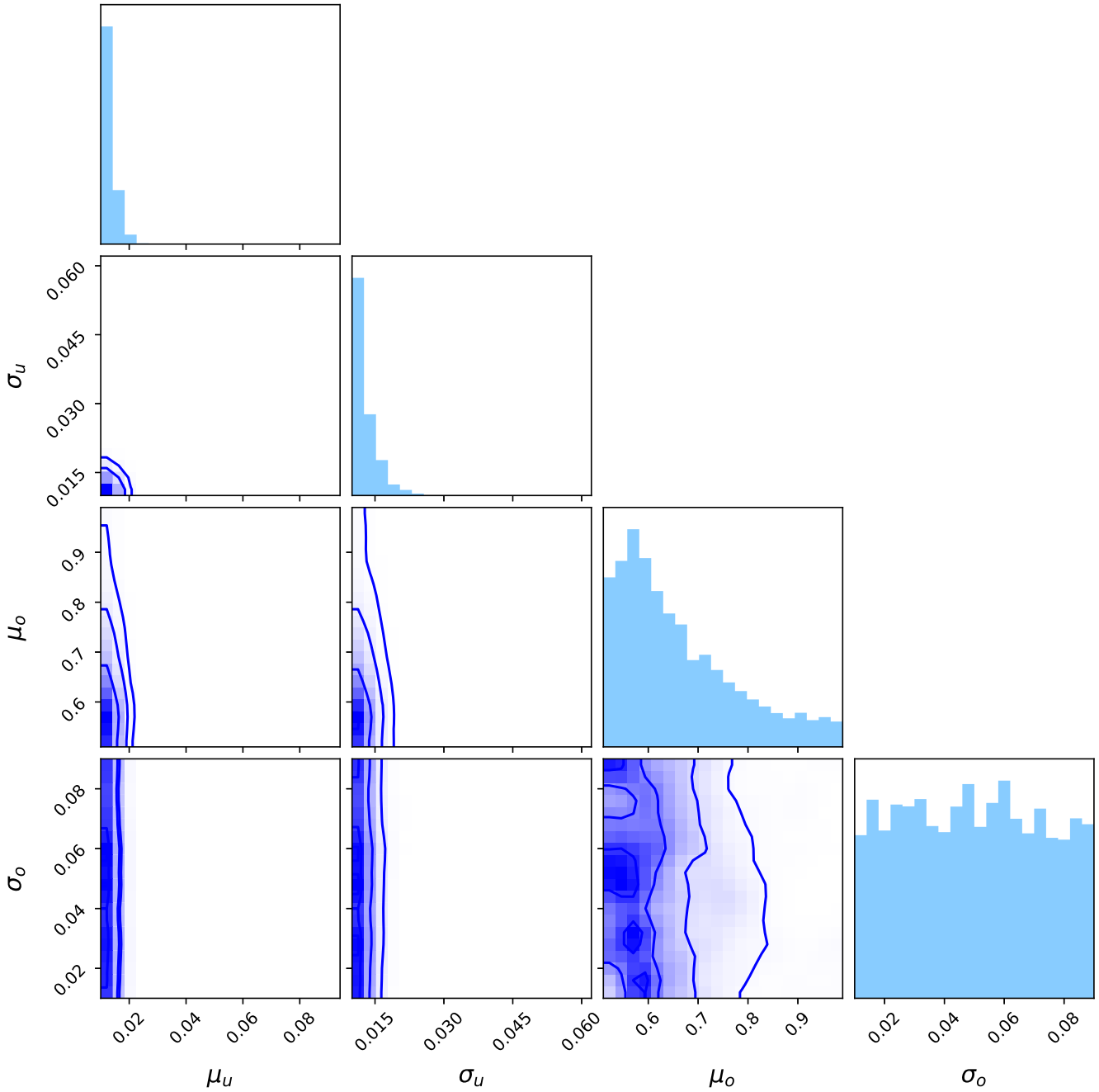

FIG. 7. Corner plot showing the MCMC result for our model carried out using the observational results of the Union 2.1 supernova Ia data [79]. The diagonal histograms show the marginalized posterior densities for each parameter.

the theoretically calculated quantity from our model $a_{\mathcal{D}}$ with the cosmological redshift, z, and the second equation [Eq. (35)] relates the theoretically calculated quantity from our model $\langle\rho\rangle_{\mathcal{D}}$ with the observational quantity, the angular diameter distance D_A. From this D_A, we can calculate the distance modulus using standard cosmological distance relations and thus compare our model with the Union 2.1 supernova Ia data.

In this analysis, the resulting posterior distributions of different parameters are obtained by the Markov chain Monte Carlo (MCMC) iteration method (Fig. 7) by using the MCMCSTAT package [80,81]. We use a total of 3×10^3 number of events with the adaptation interval of 100, within the parameter range: $\mu_u \in [0.01, 0.49]$, $\sigma_u \in [0.01, 0.09]$, $\mu_o \in [0.51, 0.99]$, and $\sigma_o \in [0.01, 0.09]$. The topmost plots of the first, second, third, and fourth columns of Fig. 7 represent the posterior distribution of the parameters μ_u, σ_u, μ_o, and σ_o, respectively, obtained by marginalizing the other parameters. The other plots of Fig. 7 show the contour representation of the posterior distribution in different sets of a two-parameter space. In these contour plots, the darker-colored regions denote higher posterior regions, and the lines indicate the boundaries of 1σ, 2σ, and 3σ regions, respectively. The diagonal panels show the 1D histogram of the posterior distribution for each model parameter obtained by marginalizing the other parameters. The off-diagonal panels show 2D projections of the posterior probability distributions for each pair of parameters and correlations between the parameters and contours.

From this analysis the obtained set of optimum points are $\mu_u = 0.01^{+0.00}_{-0.00}$, $\sigma_u = 0.01^{+0.00}_{-0.00}$, $\mu_o = 0.63^{+0.16}_{-0.08}$, and $\sigma_o = 0.05^{+0.03}_{-0.03}$, respectively. These optimum points are obtained considering all four parameters. However, from the marginalized posterior plot for μ_o (in Fig. 7), one can notice that the most probable value of μ_o is slightly lower ($\mu_o = 0.55$) than the corresponding optimal point. This is because posterior plots for each parameter plotted along the diagonal are obtained by marginalizing the other parameters. These plots do not consider other parameters; therefore, the most probable values differ from the optimum values. Similarly, the most probable values for other model parameters are $\mu_u = 0.01$, $\sigma_u = 0.01$, and $\sigma_o = 0.06$. It can be seen that lower values of σ_u, μ_u, and μ_o are favored, which in turn favors a reduced brightness temperature of the T_{21} signal, as determined from our analysis of (Figs. 4–6).

In Fig. 8, the brightness temperature T_{21} is plotted in units of mK as a function of redshift z in the range 14–20 for the ΛCDM model and for the optimal and most probable values of the parameters of our backreaction model, obtained from the MCMC analysis. The set of optimal values used is $(\mu_u, \sigma_u, \mu_o, \sigma_o) = (0.01, 0.01, 0.63, 0.05)$ and the set of most probable value used is $(\mu_u, \sigma_u, \mu_o, \sigma_o) = (0.01, 0.01, 0.55, 0.06)$. Both the most probable and optimal sets of values gives a brightness temperature considerably lower than the ΛCDM model for this redshift range.

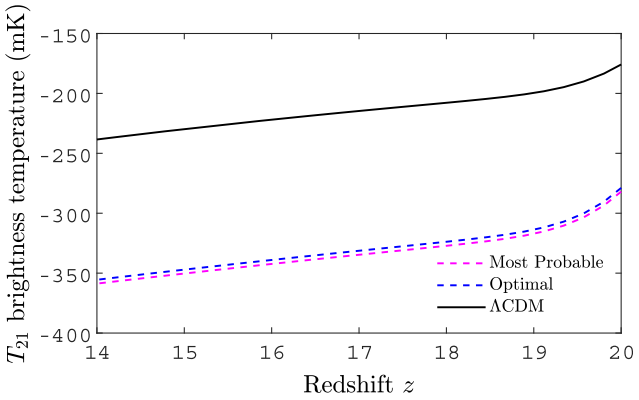

FIG. 8. Plots of brightness temperature T_{21} (mK) for the ΛCDM model and our backreaction model for the optimal values and the most probable values of our model parameters obtained from the MCMC analysis for the redshift range 14–20. Dashed plotlines are for our backreaction model.

At $z = 14$, T_{21} for our backreaction model, the optimal and most probable set of parameter values is around ≈ -350 mK, which is within the range of the EDGES result. This value is lower than the ≈ -240 mK given by the ΛCDM model.

VII. CONCLUSIONS

Recent observations indicate that our Universe contains an inhomogeneous matter distribution at considerably large scales [21–23]. The effect of these inhomogeneities on various cosmological phenomena calls for close scrutiny. In the present study, we revisit the 21-cm cosmology [1–3], in a spacetime with matter distribution inhomogeneities. We explore the brightness temperature of the 21-cm signal as a function of the redshift under the impact of backreaction from matter inhomogeneities.

In our analysis, we use the widely used Buchert formalism [29,30] of averaging over inhomogeneities to evaluate the backreaction effect. The Buchert framework facilitates the relation of theoretically evaluated quantities with observables such as redshift and angular diameter distance [41,42,56–58]. Within this framework, we construct a model of multiple subregions with a Gaussian distribution of parameters to mimic the actual Universe containing multiple voids and structures at the present epoch. We employ the covariant scheme to relate our theoretically evaluated parameters with observational quantities.

Using this model, we calculate the brightness temperature T_{21} of the 21-cm signal as a function of the redshift and analyze it for our model parameters. Such a model of spacetime that we have employed leads to a modification of the Hubble evolution, making it desirable to constrain our model parameters using observational results. To correlate our model with observation data, we obtain the marginalized posterior densities for each model parameter through MCMC simulations using Union 2.1 supernova Ia data [79].

Our analysis shows that the 21-cm brightness temperature T_{21} could be lowered by a significant amount under the impact of altered Hubble evolution resulting due to backreaction from matter distribution inhomogeneities. Such a result follows without utilizing any exotic physics or nonstandard models of dark matter and dark energy, such as schemes employed in a host of previous works [9–16] to lower the 21-cm brightness temperature. In particular, using the optimal and most probable values of our model parameters obtained through the MCMC simulations, it can be seen that T_{21} could drop to levels below the predictions of ΛCDM and within the range of the EDGES result.

We conclude by noting that several earth-based and space-based experiments have been proposed to observe and record the 21-cm signal effectively [74–78]. Our analysis obtains the evolution of T_{21} over a wide range of redshift z in Fig. 4. Thus, it can be used in conjugation with data from such experiments to analyze the role of matter distribution inhomogeneities in 21-cm cosmology. Specifically, if any dip of temperature below the ΛCDM prediction is observed in the 21-cm signal, our present analysis should motivate further detailed investigations of other backreaction scenarios [24–28] as well.

ACKNOWLEDGMENTS

The authors would like to thank the anonymous referee for insightful comments. S. S. P. would like to thank the Council of Scientific and Industrial Research (CSIR), Government of India, for funding through the CSIR-SRF-NET fellowship.

APPENDIX A: CALCULATION OF t_0

Using Eq. (17), we can break down H_D as

$$H_{\mathcal{D}} = \sum_i \lambda_{o_i} H_{o_i} + \sum_j \lambda_{u_j} H_{u_j} = \lambda_o H_o + \lambda_u H_u, \quad \text{(A1)}$$

where, $\lambda_o H_o = \sum_i \lambda_{o_i} H_{o_i}$ represents the collective contribution of overdense subregions, and similarly $\lambda_u H_u = \sum_i \lambda_{u_i} H_{u_i}$ represents the collective contribution of underdense subregions. Also, using Eq. (20), we can write

$$a_{\mathcal{D}}^3 = \lambda_{o,0} a_o^3 + \lambda_{u,0} a_u^3, \quad \text{(A2)}$$

where $\lambda_{o,0} a_o^3$ represents the collective contribution of the overdense subregions and similarly $\lambda_{u,0} a_u^3$ for the underdense subregions. Using Eq. (29), Eq. (A1) can be written as

$$\begin{aligned} H_{\mathcal{D}} &= \lambda_{o,0} \frac{a_o^3}{a_{\mathcal{D}}^3} H_o + \lambda_{u,0} \frac{a_u^3}{a_{\mathcal{D}}^3} H_u, \\ &= H_o \left(\frac{\lambda_{o,0} a_o^3}{\lambda_{o,0} a_o^3 + \lambda_{u,0} a_u^3} + \frac{\lambda_{u,0} a_u^3}{\lambda_{o,0} a_o^3 + \lambda_{u,0} a_u^3} \frac{H_u}{H_o} \right), \\ &= H_o (1 - v + vh), \end{aligned} \quad \text{(A3)}$$

where, using the definitions of h and v from [55], we have defined similarly $h \coloneqq H_u/H_o$ and $v \coloneqq \frac{\lambda_{u,0} a_u^3}{\lambda_{o,0} a_o^3 + \lambda_{u,0} a_u^3}$. Our definition of v is different from theirs due to the different scaling of $a_{\mathcal{D}}$ that we have used here. Therefore,

$$H_{\mathcal{D}} = H_o (1 - v + vh) = \frac{\sum_i \lambda_{o_i} H_{o_i}}{\lambda_o} (1 - v + vh). \quad \text{(A4)}$$

Now, using Eqs. (22) and (23),

$$H_{o_i} = \frac{\sin \phi_{o_i} (\phi_{o_i} - \sin \phi_{o_i})}{t_0 (1 - \cos \phi_{o_i})^2}. \quad \text{(A5)}$$

Therefore,

$$H_{\mathcal{D}} = \frac{1}{\lambda_o t_0} (1 - v + vh) \sum_i \lambda_{o_i} \frac{\sin \phi_{o_i} (\phi_{o_i} - \sin \phi_{o_i})}{(1 - \cos \phi_{o_i})^2}. \quad \text{(A6)}$$

At present time, t_0,

$$H_{\mathcal{D}_0} = \frac{1}{\lambda_{o,0} t_0} (1 - v_0 + v_0 h_0) \sum_i \lambda_{o_{i,0}} \frac{\sin \phi_{o_{i,0}} (\phi_{o_{i,0}} - \sin \phi_{o_{i,0}})}{(1 - \cos \phi_{o_{i,0}})^2}. \quad \text{(A7)}$$

We see that

$$\begin{aligned} t_0 = \frac{1}{\lambda_{o,0} H_{\mathcal{D}_0}} (1 - v_0 + v_0 h_0) \sum_i \lambda_{o_{i,0}} \\ \times \frac{\sin \phi_{o_{i,0}} (\phi_{o_{i,0}} - \sin \phi_{o_{i,0}})}{(1 - \cos \phi_{o_{i,0}})^2}, \end{aligned} \quad \text{(A8)}$$

so we need to fix either t_0 or $H_{\mathcal{D}_0}$. Here, we have chosen $H_{\mathcal{D}_0} = 70$ km/s/Mpc. Now we have

$$v_0 = \frac{\lambda_{u,0} a_{u,0}^3}{\lambda_{o,0} a_{o,0}^3 + \lambda_{u,0} a_{u,0}^3}, \qquad h_0 = \frac{H_{u,0}}{H_{o,0}}.$$

We have defined our model in such a way that $a_{o,0} = a_{u,0} = a_{\mathcal{D},0} = 1$. Also, $(\lambda_{o,0}, \lambda_{u,0}) = (0.09, 0.91)$ [37]. Therefore, $v_0 = 0.91$. Also,

$$\begin{aligned} \lambda_o H_o = \sum_i \lambda_{o_i} H_{o_i} \Rightarrow H_o = \frac{1}{\lambda_o} \sum_i \lambda_{o_i} H_{o_i} \\ \Rightarrow H_{o,0} = \frac{1}{\lambda_{o,0}} \sum_i \lambda_{o_i,0} H_{o_{i,0}} = \frac{1}{\lambda_{o,0} \times t_0} \sum_i \left(\frac{N_o}{\sigma_o \sqrt{2\pi}} e^{-(q_{o_{i,0}} - \mu_o)^2 / 2\sigma_o^2} \times \frac{\sin \phi_{o_{i,0}} (\phi_{o_{i,0}} - \sin \phi_{o_{i,0}})}{(1 - \cos \phi_{o_{i,0}})^2} \right) \end{aligned} \quad \text{(A9)}$$

where we have used Eq. (31). Similarly, using Eqs. (24), (25), and (30), we get the following:

$$H_{u,0}=\frac{1}{\lambda_{u,0}\times t_0}\sum_i\left(\frac{N_u}{\sigma_u\sqrt{2\pi}}e^{-(q_{u_{i,0}}-\mu_u)^2/2\sigma_u^2}\times\frac{\sinh\phi_{u_{i,0}}(\sinh\phi_{u_{i,0}}-\phi_{u_{i,0}})}{(\cosh\phi_{u_{i,0}}-1)^2}\right). \tag{A10}$$

The t_0 term in the denominators of Eqs. (A9) and (A10) cancels out and all the other quantities are known. Therefore, we have

$$h_0=\frac{H_{u,0}}{H_{o,0}}=\frac{\lambda_{o,0}}{\lambda_{u,0}}\frac{\sum_i\left(\frac{N_u}{\sigma_u\sqrt{2\pi}}e^{-(q_{u_{i,0}}-\mu_u)^2/2\sigma_u^2}\times\frac{\sinh\phi_{u_{i,0}}(\sinh\phi_{u_{i,0}}-\phi_{u_{i,0}})}{(\cosh\phi_{u_{i,0}}-1)^2}\right)}{\sum_i\left(\frac{N_o}{\sigma_o\sqrt{2\pi}}e^{-(q_{o_{i,0}}-\mu_o)^2/2\sigma_o^2}\times\frac{\sin\phi_{o_{i,0}}(\phi_{o_{i,0}}-\sin\phi_{o_{i,0}})}{(1-\cos\phi_{o_{i,0}})^2}\right)}. \tag{A11}$$

So, from Eq. (A11), we can calculate h_0 and then using this value of h_0 and v_0 in Eq. (A8), we can obtain t_0. In this way, using the above procedure, we can fix t_0 for a given set of values of our model parameters $(\mu_u,\sigma_u,\mu_o,\sigma_o)$.

APPENDIX B: OUR MULTIDOMAIN MODEL

Our multidomain model is made up of multiple subdomains of overdense and underdense. The underdense subdomains are negatively curved FLRW regions while the overdense subdomains are positively curved FLRW regions having densities greater than those of the underdense subdomains. Both of these subregions are composed of dust. Now, the scale factor for these overdense and underdense subdomains as functions of cosmic time t is given by Eqs. (22)–(25), respectively.

The densities of underdense subregions is given by [72]

$$\rho_{u_i}=\frac{\rho_{u_{i,0}}}{a_{u_i}^3}, \tag{B1}$$

where $\rho_{u_{i,0}}$ is the density at present time t_0, which is given by

$$\frac{\rho_{u_{i,0}}}{\rho_{u_{i,c}}}=q_{u_{i,0}},\quad \text{where } \rho_{u_{i,c}}=\frac{3H_{u_i,0}^2}{8\pi G}, \tag{B2}$$

where $\rho_{u_{i,c}}$ is the critical density and $H_{u_i,0}$ is the value of present time Hubble parameter for the ith underdense subregion.

Densities for the overdense subregions can also be defined similarly,

$$\rho_{o_i}=\frac{\rho_{o_{i,0}}}{a_{o_i}^3}, \tag{B3}$$

where $\rho_{o_{i,0}}$ is the density at present time t_0, which is given by

$$\frac{\rho_{o_{i,0}}}{\rho_{o_{i,c}}}=q_{o_{i,0}},\quad \text{where } \rho_{o_{i,c}}=\frac{3H_{o_i,0}^2}{8\pi G}, \tag{B4}$$

where $\rho_{o_{i,c}}$ is the critical density and $H_{o_i,0}$ is the value of present time Hubble parameter for the ith overdense subregion.

Choosing our parameters in the range $0<q_{u_{i,0}}<0.5$ and $1/2<q_{o_{i,0}}<1$, it follows from Eqs. (B2) and (B4) that the densities of underdense subdomains remain always less than the densities of overdense subdomains.

The combined density for all overdense subregions (ρ_o) is given by

$$\lambda_o\rho_o=\sum_i\lambda_{o_i}\rho_{o_i}\Rightarrow\rho_o=\frac{\sum_i\lambda_{o_i}\rho_{o_i}}{\sum_i\lambda_{o_i}}, \tag{B5}$$

where λ_{o_i} are defined in Eq. (29) and λ_o is the total volume fraction of the overdense subregions. Similarly,

$$\lambda_u\rho_u=\sum_i\lambda_{u_i}\rho_{u_i}\Rightarrow\rho_u=\frac{\sum_i\lambda_{u_i}\rho_{u_i}}{\sum_i\lambda_{u_i}}, \tag{B6}$$

where λ_{u_i} are defined in Eq. (32) and λ_u is the total volume fraction of the underdense subregions.

Also, $\langle\rho\rangle_{\mathcal{D}}$, the averaged density of the global domain is given by

$$\begin{aligned}\langle\rho\rangle_{\mathcal{D}}&=\lambda_o\rho_o+\lambda_u\rho_u,\\&=\sum_i\lambda_{o_i}\rho_{o_i}+\sum_i\lambda_{u_i}\rho_{u_i}.\end{aligned} \tag{B7}$$

The various density parameters are obtained in our analysis in the following way. From Eq. (13), we have

$$3H_{\mathcal{D}}^2=8\pi G\langle\rho\rangle_{\mathcal{D}}-\frac{1}{2}\langle\mathcal{R}\rangle_{\mathcal{D}}-\frac{1}{2}\mathcal{Q}_{\mathcal{D}}. \tag{B8}$$

Dividing by $3H_{\mathcal{D}}^2$ throughout, we get

$$1=\Omega_m^{\mathcal{D}}+\Omega_{\mathcal{R}}^{\mathcal{D}}+\Omega_{\mathcal{Q}}^{\mathcal{D}}, \tag{B9}$$

where

$$\Omega_m^{\mathcal{D}} = \frac{8\pi G\langle\rho\rangle_{\mathcal{D}}}{3H_{\mathcal{D}}^2}, \qquad \Omega_{\mathcal{R}}^{\mathcal{D}} = -\frac{\langle\mathcal{R}\rangle_{\mathcal{D}}}{6H_{\mathcal{D}}^2}, \qquad \Omega_{\mathcal{Q}}^{\mathcal{D}} = -\frac{\mathcal{Q}_{\mathcal{D}}}{6H_{\mathcal{D}}^2}. \tag{B10}$$

From Eq. (33), we can calculate $\mathcal{Q}_{\mathcal{D}}$ for our model and then from Eq. (B10), $\Omega_{\mathcal{Q}}^{\mathcal{D}}$ can be calculated. Then using, Eqs. (B7) and (B10), $\Omega_m^{\mathcal{D}}$ can be calculated and $\Omega_{\mathcal{R}}^{\mathcal{D}}$ can be calculated from Eq. (B9). In this way, all the average density parameters can be obtained.

[1] S. R. Furlanetto, S. Peng Oh, and F. H. Briggs, Cosmology at low frequencies: The 21 cm transition and the high-redshift universe, Phys. Rep. **433**, 181 (2006).

[2] M. F. Morales and J. S. B. Wyithe, Reionization and cosmology with 21-cm fluctuations, Annu. Rev. Astron. Astrophys. **48**, 127 (2010).

[3] J. R. Pritchard and A. Loeb, 21 cm cosmology in the 21st century, Rep. Prog. Phys. **75**, 086901 (2012).

[4] H. I. Ewen and E. M. Purcell, Observation of a line in the galactic radio spectrum: Radiation from galactic hydrogen at 1,420 mc./sec., Nature (London) **168**, 356 (1951).

[5] C. A. Muller and J. H. Oort, Observation of a line in the galactic radio spectrum: The interstellar hydrogen line at 1,420 mc./sec., and an estimate of galactic rotation, Nature (London) **168**, 357 (1951).

[6] J. D. Bowman, A. E. E. Rogers, R. A. Monsalve, T. J. Mozdzen, and N. Mahesh, An absorption profile centred at 78 megahertz in the sky-averaged spectrum, Nature (London) **555**, 67 (2018).

[7] S. Singh *et al.*, Saras 2 constraints on global 21 cm signals from the epoch of reionization*, Astrophys. J. **858**, 54 (2018).

[8] S. Singh, J. Nambissan T., R. Subrahmanyan, N. U. Shankar, B. S. Girish, A. Raghunathan, R. Somashekar, K. S. Srivani, and M. S. Rao, On the detection of a cosmic dawn signal in the radio background, Nat. Astron. **6**, 607 (2022).

[9] A. Halder and M. Pandey, Probing the effects of primordial black holes on 21-cm EDGES signal along with interacting dark energy and dark matter-baryon scattering, Mon. Not. R. Astron. Soc. **508**, 3446 (2021).

[10] A. Halder and S. Banerjee, Bounds on abundance of primordial black hole and dark matter from edges 21-cm signal, Phys. Rev. D **103**, 063044 (2021).

[11] A. Halder, M. Pandey, D. Majumdar, and R. Basu, Exploring multimessenger signals from heavy dark matter decay with edges 21-cm result and IceCube, J. Cosmol. Astropart. Phys. 10 (2021) 033.

[12] S. J. Clark, B. Dutta, Y. Gao, Y.-Z. Ma, and L. E. Strigari, 21 cm limits on decaying dark matter and primordial black holes, Phys. Rev. D **98**, 043006 (2018).

[13] U. Mukhopadhyay, D. Majumdar, and K. K. Datta, Probing interacting dark energy and scattering of baryons with dark matter in light of the edges 21-cm signal, Phys. Rev. D **103**, 063510 (2021).

[14] Y. Yang, Constraints on primordial black holes and curvature perturbations from the global 21-cm signal, Phys. Rev. D **102**, 083538 (2020).

[15] J. B. Muñoz, E. D. Kovetz, and Y. Ali-Haïmoud, Heating of baryons due to scattering with dark matter during the dark ages, Phys. Rev. D **92**, 083528 (2015).

[16] A. Halder, S. S. Pandey, and A. Majumdar, Global 21-cm brightness temperature in viscous dark energy models, J. Cosmol. Astropart. Phys. 10 (2022) 049.

[17] A. K. Saha and R. Laha, Sensitivities on nonspinning and spinning primordial black hole dark matter with global 21-cm troughs, Phys. Rev. D **105**, 103026 (2022).

[18] M. Chianese, P. Di Bari, K. Farrag, and R. Samanta, Probing relic neutrino radiative decays with 21 cm cosmology, Phys. Lett. B **790**, 64 (2019).

[19] A. G. Riess, S. Casertano, W. Yuan, J. B. Bowers, L. Macri, J. C. Zinn, and D. Scolnic, Cosmic distances calibrated to 1% precision with Gaia EDR3 parallaxes and Hubble Space Telescope photometry of 75 milky way cepheids confirm tension with λCDM, Astrophys. J. Lett. **908**, L6 (2021).

[20] W. L. Freedman, Measurements of the Hubble constant: Tensions in perspective*, Astrophys. J. **919**, 16 (2021).

[21] F. S. Labini, N. L. Vasilyev, L. Pietronero, and Y. V. Baryshev, Absence of self-averaging and of homogeneity in the large-scale galaxy distribution, Europhys. Lett. **86**, 49001 (2009).

[22] A. Wiegand, T. Buchert, and M. Ostermann, Direct Minkowski functional analysis of large redshift surveys: A new high-speed code tested on the luminous red galaxy Sloan Digital Sky Survey-DR7 catalogue, Mon. Not. R. Astron. Soc. **443**, 241 (2014).

[23] A. M. Lopez, R. G. Clowes, and G. M. Williger, A giant arc on the sky, Mon. Not. R. Astron. Soc. **516**, 1557 (2022).

[24] G. F. R. Ellis, Relativistic cosmology: Its nature, aims and problems, in *General Relativity and Gravitation: Invited Papers and Discussion Reports of the 10th International Conference on General Relativity and Gravitation, Padua, 1983*, edited by B. Bertotti, F. de Felice, and A. Pascolini (Springer Netherlands, Dordrecht, 1984), pp. 215–288.

[25] T. Futamase, Approximation scheme for constructing a clumpy universe in general relativity, Phys. Rev. Lett. **61**, 2175 (1988).

[26] R. M. Zalaletdinov, Averaging out the Einstein equations, Gen. Relativ. Gravit. **24**, 1015 (1992).

[27] R. M. Zalaletdinov, Towards a theory of macroscopic gravity, Gen. Relativ. Gravit. **25**, 673 (1993).
[28] M. Gasperini, G. Marozzi, F. Nugier, and G. Veneziano, Light-cone averaging in cosmology: Formalism and applications, J. Cosmol. Astropart. Phys. 07 (2011) 008.
[29] T. Buchert, On average properties of inhomogeneous fluids in general relativity: Dust cosmologies, Gen. Relativ. Gravit. **32**, 105 (2000).
[30] T. Buchert, On average properties of inhomogeneous fluids in general relativity: Perfect fluid cosmologies, Gen. Relativ. Gravit. **33**, 1381 (2001).
[31] A. A. Coley, N. Pelavas, and R. M. Zalaletdinov, Cosmological solutions in macroscopic gravity, Phys. Rev. Lett. **95**, 151102 (2005).
[32] M. Korzyński, Covariant coarse graining of inhomogeneous dust flow in general relativity, Classical Quantum Gravity **27**, 105015 (2010).
[33] T. Clifton, K. Rosquist, and R. Tavakol, An exact quantification of backreaction in relativistic cosmology, Phys. Rev. D **86**, 043506 (2012).
[34] H. Skarke, Inhomogeneity implies accelerated expansion, Phys. Rev. D **89**, 043506 (2014).
[35] T. Buchert, M. Carfora, G. F. R. Ellis, E. W. Kolb, M. A. H. MacCallum, J. J. Ostrowski, S. Räsänen, B. F. Roukema, L. Andersson, A. A. Coley, and D. L. Wiltshire, Is there proof that backreaction of inhomogeneities is irrelevant in cosmology?, Classical Quantum Gravity **32**, 215021 (2015).
[36] T. Buchert, A. A. Coley, H. Kleinert, B. F. Roukema, and D. L. Wiltshire, Observational challenges for the standard FLRW model, Int. J. Mod. Phys. D **25**, 1630007 (2016).
[37] A. Wiegand and T. Buchert, Multiscale cosmology and structure-emerging dark energy: A plausibility analysis, Phys. Rev. D **82**, 023523 (2010).
[38] S. Räsänen, Dark energy from back-reaction, J. Cosmol. Astropart. Phys. 02 (2004) 003.
[39] D. L. Wiltshire, Dark energy without dark energy, in *Dark Matter in Astroparticle and Particle Physics* (World Scientific, 2008), pp. 565–596.
[40] E. W. Kolb, S. Matarrese, and A. Riotto, On cosmic acceleration without dark energy, New J. Phys. **8**, 322 (2006).
[41] S. Koksbang, Another look at redshift drift and the backreaction conjecture, J. Cosmol. Astropart. Phys. 10 (2019) 036.
[42] S. M. Koksbang, Observations in statistically homogeneous, locally inhomogeneous cosmological toy models without FLRW backgrounds, Mon. Not. R. Astron. Soc. **498**, L135 (2020).
[43] S. M. Koksbang, Searching for signals of inhomogeneity using multiple probes of the cosmic expansion rate $h(z)$, Phys. Rev. Lett. **126**, 231101 (2021).
[44] S. Räsänen, Evaluating backreaction with the peak model of structure formation, J. Cosmol. Astropart. Phys. 04 (2008) 026.
[45] N. Bose and A. S. Majumdar, Future deceleration due to cosmic backreaction in presence of the event horizon, Mon. Not. R. Astron. Soc. **418**, L45 (2011).
[46] N. Bose and A. S. Majumdar, Effect of cosmic backreaction on the future evolution of an accelerating universe, Gen. Relativ. Gravit. **45**, 1971 (2013).
[47] A. Ali and A. Majumdar, Future evolution in a backreaction model and the analogous scalar field cosmology, J. Cosmol. Astropart. Phys. 01 (2017) 054.
[48] S. S. Pandey, A. Sarkar, A. Ali, and A. Majumdar, Effect of inhomogeneities on the propagation of gravitational waves from binaries of compact objects, J. Cosmol. Astropart. Phys. 06 (2022) 021.
[49] S. S. Pandey, A. Sarkar, A. Ali, and A. S. Majumdar, Viscous attenuation of gravitational waves propagating through an inhomogeneous background, Eur. Phys. J. C **83**, 435 (2023).
[50] S. Koksbang and S. Hannestad, Redshift drift in an inhomogeneous universe: Averaging and the backreaction conjecture, J. Cosmol. Astropart. Phys. 01 (2016) 009.
[51] S. M. Koksbang, Quantifying effects of inhomogeneities and curvature on gravitational wave standard siren measurements of $h(z)$, Phys. Rev. D **106**, 063514 (2022).
[52] S. M. Koksbang, Cosmic backreaction and the mean redshift drift from symbolic regression, Phys. Rev. D **107**, 103522 (2023).
[53] S. M. Koksbang, Machine learning cosmic backreaction and its effects on observations, Phys. Rev. Lett. **130**, 201003 (2023).
[54] A. Halder, S. S. Pandey, and A. Majumdar, Future deceleration due to backreaction in a universe with multiple inhomogeneous domains, J. Cosmol. Astropart. Phys. 08 (2023) 064.
[55] S. M. Koksbang, Cosmic backreaction and the mean redshift drift from symbolic regression, Phys. Rev. D **107**, 103522 (2023).
[56] S. Räsänen, Light propagation in statistically homogeneous and isotropic dust universes, J. Cosmol. Astropart. Phys. 02 (2009) 011.
[57] S. Räsänen, Light propagation in statistically homogeneous and isotropic universes with general matter content, J. Cosmol. Astropart. Phys. 03 (2010) 018.
[58] S. M. Koksbang, Towards statistically homogeneous and isotropic perfect fluid universes with cosmic backreaction, Classical Quantum Gravity **36**, 185004 (2019).
[59] S. Koksbang, On the relationship between mean observations, spatial averages and the Dyer-Roeder approximation in Einstein-Straus models, J. Cosmol. Astropart. Phys. 11 (2020) 061.
[60] J. B. Muñoz, E. D. Kovetz, and Y. Ali-Haïmoud, Heating of baryons due to scattering with dark matter during the dark ages, Phys. Rev. D **92**, 083528 (2015).
[61] Y. Ali-Haïmoud and C. M. Hirata, Ultrafast effective multilevel atom method for primordial hydrogen recombination, Phys. Rev. D **82**, 063521 (2010).
[62] M. Zaldarriaga, S. R. Furlanetto, and L. Hernquist, 21 centimeter fluctuations from cosmic gas at high redshifts, Astrophys. J. **608**, 622 (2004).
[63] S. A. Wouthuysen, On the excitation mechanism of the 21-cm (radio-frequency) interstellar hydrogen emission line, Astron. J. **57**, 31 (1952).
[64] G. B. Field, Excitation of the hydrogen 21-cm line, Proc. IRE **46**, 240 (1958).
[65] M. Kuhlen, P. Madau, and R. Montgomery, The spin temperature and 21 cm brightness of the intergalactic medium in the pre-reionization era, Astrophys. J. **637**, L1 (2006).

[66] C. M. Hirata, Wouthuysen-Field coupling strength and application to high-redshift 21-cm radiation, Mon. Not. R. Astron. Soc. **367**, 259 (2006).
[67] B. Ciardi and P. Madau, Probing beyond the epoch of hydrogen reionization with 21 centimeter radiation, Astrophys. J. **596**, 1 (2003).
[68] Y. Ali-Haïmoud and C. M. Hirata, HyRec: A fast and highly accurate primordial hydrogen and helium recombination code, Phys. Rev. D **83**, 043513 (2011).
[69] M. S. Madhavacheril, N. Sehgal, and T. R. Slatyer, Current dark matter annihilation constraints from CMB and low-redshift data, Phys. Rev. D **89**, 103508 (2014).
[70] P. J. E. Peebles, Recombination of the primeval plasma, Astrophys. J. **153**, 1 (1968).
[71] T. Buchert and S. Räsänen, Backreaction in late-time cosmology, Annu. Rev. Nucl. Part. Sci. **62**, 57 (2012).
[72] S. Weinberg, *Gravitation and Cosmology: Principles and Applications of the General Theory of Relativity* (John Wiley and Sons, New York, 1972).
[73] S. Räsänen, Accelerated expansion from structure formation, J. Cosmol. Astropart. Phys. 11 (2006) 003.
[74] J. O. Burns *et al.*, A space-based observational strategy for characterizing the first stars and galaxies using the redshifted 21 cm global spectrum, Astrophys. J. **844**, 33 (2017).
[75] J. O. Burns, J. Lazio, S. Bale, J. Bowman, R. Bradley, C. Carilli, S. Furlanetto, G. Harker, A. Loeb, and J. Pritchard, Probing the first stars and black holes in the early universe with the dark ages radio explorer (dare), Adv. Space Res. **49**, 433 (2012).
[76] M. Sathyanarayana Rao *et al.*, Pratush experiment concept and design overview, Exp. Astron. **56**, 741 (2023).
[77] J. Cumner *et al.*, Radio antenna design for sky-averaged 21 cm cosmology experiments: The reach case, J. Astron. Instrum. **11**, 2250001 (2022).
[78] M. Sokolowski *et al.*, Bighorns—broadband instrument for global hydrogen reionisation signal, Publ. Astron. Soc. Aust. **32**, e004 (2015).
[79] N. Suzuki *et al.*, The Hubble Space Telescope cluster supernova survey. V. Improving the dark-energy constraints above $z > 1$ and building an early-type-hosted supernova sample*, Astrophys. J. **746**, 85 (2012).
[80] H. Haario, M. Laine, A. Mira, and E. Saksman, DRAM: Efficient adaptive MCMC, Stat. Comput. **16**, 339 (2006).
[81] H. Haario, E. Saksman, and J. Tamminen, An adaptive metropolis algorithm, Bernoulli **7**, 223 (2001).